IOWA STATE UNIVERSITY
Digital Repository

Graduate Theses and Dissertations

Iowa State University Capstones, Theses and Dissertations

2016

Reducing uncertainty in wind turbine blade health inspection with image processing techniques

Huiyi Zhang
Iowa State University

Follow this and additional works at: https://lib.dr.iastate.edu/etd

Part of the Industrial Engineering Commons, and the Oil, Gas, and Energy Commons

Recommended Citation

Zhang, Huiyi, "Reducing uncertainty in wind turbine blade health inspection with image processing techniques" (2016). *Graduate Theses and Dissertations*. 15207.
https://lib.dr.iastate.edu/etd/15207

This Dissertation is brought to you for free and open access by the Iowa State University Capstones, Theses and Dissertations at Iowa State University Digital Repository. It has been accepted for inclusion in Graduate Theses and Dissertations by an authorized administrator of Iowa State University Digital Repository. For more information, please contact digirep@iastate.edu.

المنارة للاستشارات

www.manaraa.com

Reducing uncertainty in wind turbine blade health inspection with image processing techniques

by

Huiyi Zhang

A dissertation submitted to the graduate faculty

in partial fulfillment of the requirements for the degree of

DOCTOR OF PHILOSOPHY

Major: Wind Energy Science, Engineering, and Policy

Program of Study Committee:

John Jackman, Major Professor
William Meeker
Viney Dayal
Matthew Frank
Frank Peters

Iowa State University

Ames, Iowa

2016

Copyright © Huiyi Zhang, 2016. All rights reserved.

TABLE OF CONTENTS

ABSTRACT

Structural health inspection has been widely applied in the operation of wind farms to find early cracks in wind turbine blades (WTBs). Increased numbers of turbines and expanded rotor diameters are driving up the workloads and safety risks for site employees. Therefore, it is important to automate the inspection process as well as minimize the uncertainties involved in routine blade health inspection. In addition, crack documentation and trending is vital to assess rotor blade and turbine reliability in the 20 year designed life span. A new crack recognition and classification algorithm is described that can support automated structural health inspection of the surface of large composite WTBs. The first part of the study investigated the feasibility of digital image processing in WTB health inspection and defined the capability of numerically detecting cracks as small as hairline thickness. The second part of the study identified and analyzed the uncertainty of the digital image processing method. A self-learning algorithm was proposed to recognize and classify cracks without comparing a blade image to a library of crack images. The last part of the research quantified the uncertainty in the field conditions and the image processing methods.

CHAPTER 1. GENERAL INTRODUCTION

1.1 Background

Given the rapid increase in the number of commercialized multi-hundred megawatt (MW) wind farms, on-site health inspection of wind turbine blades (WTBs) has become more challenging, costly, and time consuming. This study focuses on investigating an image processing-based semi-automatic method to identify early defects on WTBs using algorithms that address the uncertainties involved in the inspection method so that surface defects can be identified accurately and in a timely manner. This chapter explains the necessity of improving early defect inspection accuracy on WTBs.

Wind technology has improved dramatically in the past decade (2001 – 2013) with the average wind turbine nameplate capacity increasing from 1MW to 2MW and the average rotor diameter increasing from 50 meters to 100 meters [1]. Leading manufacturers and research institutes have been proposing and deploying even larger wind turbines with longer blades in recent years such as the 62.5-m long Innoblades designed by Gamesa and the 83.5-m long blades from Danish SSP Technology that have been installed on a 7 MW offshore turbine for Samsung Heavy Industry [2]. The continuously growing rotor diameter adds significant challenges to blade inspection and maintenance due to its large scale and location on an elevated tower. Meanwhile, blades are expensive components where the installation cost of WTBs is linearly proportional to the rotor diameter and typically accounts for 10-20% of the total installation cost when the blade length is at 10-50 meters [3]. In addition, wind turbine blades are not "fit and forget" components since their failure rate ranks in the top third among all critical large mechanical components. Further, a blade failure brings significant down time, 4 days on average, that requires expensive cranes and skilled technicians to make repairs [4]. Additionally, repair plans must be developed and approved by experienced engineers, which adds to the maintenance cost. Detecting blade failures in their early stages can offer engineers more time to propose the most cost-effective solution, such as deciding whether to repair as soon as possible or to carefully operate the turbine until the low wind speed season comes. More importantly, detecting early defects can prevent severe structural failure, including catastrophic failure, which typically requires blade replacement and significantly reduces the availability of the turbine.

Turbine blades are made of fiber reinforced composite materials and finished with a gelcoat layer and a protective paint. The gelcoat layer is typically made of epoxy resin or polyester resin that can prevent the infiltration of moisture, dust, and salt into the underlying fiber reinforced composite material [5]. Early defects appeared along the coating layers as small cracks or erosion. Meanwhile, structural damage may also be seen along the surface coating layers such as lightning damage where the first sign of cracks appears near the tip of the blade [6]. Thus, it is critical to detect early cracks along the surface coating layers. From these, the engineer can formulate further inspection, operation, and repair plans. For example, the engineer will not send crew on tower to perform structural health inspection without sufficient insight from the turbine operational condition and the blade visual health inspection since structural health inspection is more expensive and adds down time to the turbine. Therefore, it is necessary to study new methods that can inspect gel goat layer defects efficiently and accurately.

1.2 Motivation

WTBs require routine visual inspection to find cracks, leading edge erosion, and severe surface roughness, all of which negatively impact turbine performance and may lead to severe structural problems. Ground-based inspection using telescopes introduce significant uncertainty because of variations in inspector skill and the effects of eyestrain and fatigue [7]. Digital images and digital image processing techniques are key components of automated optical inspection techniques. In recent years, researchers have been working on semi-automatic or robotic methods for detecting blade surface flaws to improve the accuracy of inspection results, reduce safety concerns, and replace current practices such as platform-based inspection or sky workers [8-11]. Thorough surface and structural inspections are performed using platform-based inspection or sky workers. These inspections usually require nondestructive devices and are more expensive than routine visual inspection, which most frequently occurs near the end of warranty, once a year for older blades, or whenever severe damage occurs.

New automated inspection methods are needed to address the shortcomings of current techniques and the increased demand for inspection due to the rapid increase in wind turbine installations. These methods should reduce inspection time and cost as well as improve the reliability of the results, especially in minimizing inspection time on tower. Given the increased emphasis on developing offshore wind farms, remotely controlled inspection methods are preferred to sending maintenance teams offshore because of cost and safety concerns for workers [12].

Among all the proposed techniques, image segmentation is an effective way to extract flaws like cracks from digital images of the WTBs rather than identifying the defects with the human eye [13]. Thus, reducing the uncertainties involved in image segmentation will improve the efficacy of automated blade inspection technologies.

Current proposed automated or semi-automated blade inspection methods use two different approaches: (1) sending a climbing device on tower (or on the blades) while the blades are stationary and (2) an unmanned aerial vehicle (UAV) which is affected by wind speed and fluctuations in wind direction. Both of these approaches require image segmentation to extract defects from recorded images of blade surfaces. Moreover, both approaches need some form of registration to locate the defect locations on a blade (and therefore, it is necessary to identify the location of the blades and the orientation of the nacelle). Otherwise, the inspection methods will be highly dependent on the skill of the on-site operator and the location of defects will have a high degree of uncertainty.

MATLAB defines image segmentation as a “process of dividing an image into multiple parts [that] is typically used to identify objects or other relevant information in digital images.” [14] Thus, image segmentation techniques can identify the orientation of a wind turbine nacelle and recognize the position of each blade with respect to the plane of the rotor. This is a critical step in a fully automated inspection method because the nacelle is yawing automatically following the direction of the wind and the blades are swinging slightly when the wind speed is lower than the cut-in speed (i.e., when the wind speed is less than 3 m/s). One alternative is to extract the nacelle orientation and blade position from the Supervisory Control and Data Acquisition (SCADA) system. However, this can introduce security concerns for the wind power generation owner and operators. In addition, the inspection system would be more complex because it would have to be compatible with different proprietary control systems from different wind turbine manufacturers. Therefore, using image segmentation to identify the orientation and location of the blades as well as to detect surface flaws is well suited for a cost-effective inspection system.

1.3 Research Problem

Thus the research problem is how to accurately detect WTB surface flaws like cracks and erosion in a cost-effective manner. This is important since the detection results will directly affect the operation cost, repair methods and cost, and the turbine lifetime. This study investigated the uncertainties in WTB health inspection techniques that use digital images to identify defects like cracks and erosion. By understanding the nature of these uncertainties, noise generated from the field environment as well as the image processing method itself can be identified. The findings of the study were used to develop and validate methods that reduce uncertainties and improve blade inspection results. In order to address this problem, the following three questions were addressed:

Research Question 1: Is it feasible to identify wind turbine blade surface flaws with image processing techniques rather than the human eye?

Research Question 2: What are the uncertainty parameters that need to be addressed for blade health inspections and can an image-processing model be formulated that reduces the uncertainty of image processing results while identifying blade surface flaws?

Research Question 3: What are the elements that have impact on the uncertainties of the model and can be improved for real-time on-site inspection and how are they related?

1.4 Research Objectives

The primary objective of this research is to formulate and validate image segmentation models that can accurately identify WTB surface defects onsite and under field conditions that include uneven lighting and environmental noise like insects as well as noise generated from image processing techniques. This research aims to characterize the uncertainty so that more effective inspection techniques can be developed with image processing techniques.

The first sub-objective was to investigate whether image processing methods are feasible to inspect flaws of a wind turbine blade. If this approach is feasible, the goal was identifying the image processing methods and addressing the factors that affect the inspection results.

The second sub-objective was formulating an image-processing model that can detect blade surface defects and minimize the uncertainty parameters that affect the inspection results at the same time. The goal was to understand the general uncertainty parameters such as background noise and their behaviors in the image processing model. An effective image-processing model must eliminate the noise generated from the uncertainty parameters.

The third sub-objective was to further design an algorithm that can significantly improve the inspection results from the image processing model under complex field conditions. The goal is to cover severe uncertainty sources in the field conditions so that the inspection method can be adapted to an automated inspection device. This step is critical because field conditions are more complex than lab environments. As a first step, we defined the worst-case scenarios of each field condition and studied its effects in a lab environment. It was also necessary to determine the detectability of the proposed method. Here detectability means the minimum size of a crack that can be detected with image processing techniques. False positive inspection results will add inspection costs by unnecessarily sending technicians on tower while missing an early defect can lead to potential structural damage that will increase operation and maintenance (O&M) costs significantly.

1.5 Impact

The accuracy of blade inspection results has a direct impact on the lifetime of blades, inspection and maintenance costs, and the annual energy production of a turbine. WTBs are typically designed for a 20-25 year lifetime and account for 18-20% of the turbine cost (i.e., more than $300,000). Missing defects can lead to severe problems that could result in replacing a blade and significantly increase O&M costs and decrease energy production. A healthy blade that is erroneously flagged with defects will add additional inspection costs by sending maintenance personnel on tower and reduce energy production revenue.

The methods investigated in this study can be adapted to other contexts of image segmentation methods such as satellite image segmentation and medical image segmentation. A broader impact of this research is that this study will benefit both the wind energy industry and society by decreasing the cost of wind energy because of reduced O&M costs and greater turbine reliability. With wind energy going offshore, some of the safety and cost challenges of O&M associated with sending maintenance teams on site can be addressed by automated inspection techniques.

1.6 Dissertation Organization

The remainder of this dissertation is organized as follows: Chapter 2 provides a literature review of relevant research. Chapter 3 introduces the feasibility of identifying cracks with digital image processing methods. Chapter 4 classifies the types of cracks along the coating materials of WTBs and describes a new threshold-based method with a linkage algorithm to better detect early cracks. Chapter 5 proposes a crack reorganization and classification method based on the geometric characteristics of connected pixels. Chapter 6 discusses the uncertainties in field operation. An adaptive window size thresholding was applied to eliminate the uncertainties of field conditions and the uncertainties within the digital image processing method. Finally, Chapter 7 offers a discussion of the results, concluding remarks, and an explanation of the contribution of the work.

1.7 References

[1] J. Zayas, M. Derby, P. Gilman, and S. Ananthan, Enabling wind power nationwide, May, 2015 U.S. Department of Energy. pp. 8

[2] K. Schultz, World’s largest wind turbine blades made in Denmark, Ministry of Foreign Affairs of Demark, Aug. 06th, 2013, available on-line at http://www.investindk.com/News-and-events/News/2013/Worlds-Longest-Wind-Turbine-Blades

[3] D. Berry, and S. Lockard, Cost study for large wind turbine blades, Sandia Report: SAND2003 – 1428, May. 2003. pp. 33

[4] B. Hahn, (1999). “Reliability Assessment of Wind Turbines in Germany.” 1999 European Wind Energy Conference, Nice, France, March 1-5.

[5] Bir GS., Computerized method for preliminary structural design of composite wind turbine blades. *ASME. J. Sol. Energy Eng*. 2001; Vol. 123(4), pp. 372 - 381

[6] Y. Wang and O.I. Zhupanska, Lighting strike thermal damage model for glass fiber reinforced polymer matrix composites and its application to wind turbine blades. *Composite Structures*, Vol. 132, Nov. 15th , 2015, pp. 1182 – 1191

[7] R. J. E. Hanson, Visual fatigue and eye strain in the use of telescopes. *Transactions of the Optical Society*, Vol. 22, Iss. 1, pp. 26, 1920.

[8] S. Høglund. *“Autonomous Inspection of Wind Turbines and Buildings using an UAV.”* Thesis, Norwegian University of Science and Technology, 2014. URI: urn:nbn:no:ntnu:diva-25877.

[9] M. Stokkeland. *“A Computer Vision Approach for Autonomous Wind Turbine Inspection using a Multicopter.”* Thesis, Norwegian University of Science and Technology, 2014. URI: urn:nbn:no:ntnu:diva-26126.

[10] GE Global Research. “GE Advances Wind Turbine Inspection Through Successful Robotic Trial." Internet: http://www.reuters.com/article/idUS140970+13-Jun-2012+BW2012 0613, June 13, 2012 [Oct. 8, 2014].

[11] T. P. Sattar, H. L. Rodriguez, and B. Bridge, Climbing ring robot for inspection of offshore wind turbines. *Industrial Robot: An International Journal*, vol. 36, iss: 4, pp. 326–330, 2009.

[12] H. Zhang and J. Jackman, Feasibility of Automatic Detection of Surface Cracks in Wind Turbine Blades. *Wind Engineering*, vol. 38, no. 6, pp. 575-586, 2014.

[13] H. Zhang and J. Jackman, A feasibility study of wind turbine blade surface crack detection using an optical inspection method. *Renewable Energy Research and Apllications (ICRERA), 2013 International Conference on*, DOI: 10.1109/ICRERA.2013.6749869. pp 847–852, 2013.

[14] MATLAB, Image Segmentation Available on-line at http://www.mathworks.com/discovery/image-segmentation.html. Dec. 26, 2015

CHAPTER 2. LITERATURE REVIEW

This chapter reviews previous research in three sections: threshold-based image processing, uncertainty in threshold-based image processing, and crack recognition and classification studies.

2.1 Threshold-based image processing

Thresholding image segmentation is a powerful technique in image processing in which the objects of interest are separated from the background with bilevel or multilevel thresholds. Bilevel thresholding has one threshold that segments the image into objects and background. Multilevel thresholding has several thresholds that separate the image into background and several objects corresponding to different levels of intensity regions. Both bilevel and multilevel thresholding can be applied to grayscale images. The segmented image reduces storage space significantly and can improve processing speed. However, uneven lighting causes information loss and generates Type II error (i.e., missing objects) that has been studied in recent years [1-3], especially during field inspection under uneven lighting.

Otsu’s method is one of the widely used methods for bilevel thresholding. It maximizes the variance between the two classes (background and objects) and minimizes the variance within each class so that it can provide satisfactory segmenting results even when the histogram of a grayscale image does not have two obvious peaks (i.e., the difference in intensity levesl between background and object is unclear). Many proposed methods for addressing uneven lighting have used Otsu’s method in subimages or small windows of the original images locally and then combined the segmenting results. For example, Huang developed an adaptive window size algorithm based on a pyramid data structure manipulation of the Lorentz information measure (LIM) [1]. A contour map image and a document image were tested with Huang’s method and the results showed significant improvement under uneven lighting as compared to Otsu's method.

2.2 Uncertainty in threshold-based image processing

Uncertainty from image segmentation has been studied in the context of medical image processing. Noise from the image capturing process such as uneven lighting contributes to the uncertainty of image processing and the partial volume effect is a recognized problem in medical image processing. The partial volume effect is the loss of apparent activity in small objects or regions because of the limited resolution of the imaging (i.e., a defect (e.g. a crack) is relatively small compared to the overall object (e.g. blade surface) in the image and thus it has a fuzzy outside contour/edge). Apparent activity is a technical term in image processing technics used for medical images that represents the exposure rate of the image at a distance of 1 m. Lelandais proposed a method to address both of these shortcomings based on image fusion that uses belief function theory in image segmentation. The method was validated with simulated images as well as medical images to show its ability to accurately extract images with noise and the partial volume effect. The simulated images in the study were created with different signal-to-noise ratios. These images did not have severe noise generated from the image acquisition system. Thus, the same method is expected to produce very different results for images of wind turbine blades [4].

Zhao investigated data quality and uncertainty in a geoinformation science context by modeling a set of results from image segmentation of an earth image as statistically random sets (i.e., a set of data with no recognizable patterns). A region-growing algorithm was used to quantify the extensional uncertainty (i.e., uncertainty of identifying the edges of an object in an image) of the sharp and/or vague boundaries of objects in digital images. The method was validated with 14 image objects with varying boundaries and the results were promising. However, its applicability to images with uneven illumination and severe background noise has not been studied. Also, the method targeted large-scale objects (with respect to the entire image) such as rivers and lakes, rather than small-scale objects like cracks on a blade surface [5].

In recent years, Tsai proposed an adaptive local thresholding method using simulated annealing to solve the difficulty of selecting the initial window size for Huang’s method [6]. Kanungo used a parallel genetic algorithm-based adaptive thresholding method to select the initial window size of Huang’s method. The adaptive window size segmenting methods address the uneven lighting problems but also add computational work and the initial window size problem. One possibility is that the window size will correspond to the entire image when the object is small relative to the image. Wu proposed a method based on image data fields inspired by the physical world that segments grayscale images efficiently and effectively [3]. Other studies like Ma showed that the fuzzy C-means image segmentation algorithm can solve the uneven illumination patterns when active or structured light patterns are projected onto a scene [6-8].

2.3 Automated crack recognition and classification

Defect recognition and classification were studied during the development of computer numerical controlled (CNC) machines, in which machine vision was used to select qualified materials. The wood machining applied an inspection algorithm to the CNC machine so that it could find defects in the wood materials [9]. The algorithm measures the gauging tonal properties such as the mean, the variance, the skewness, and the kurtosis of the distributions of the intensity level of pixels along the digital images of the wood surfaces. Then the algorithm computes the gauging pattern qualities and applies two pattern recognition methods for identifying defects along the wood surfaces. One of them is a pairwise multiclass classification scheme that determines whether an entire part of the surface image is within the bounds of a standard chi-squared test. However, the accuracy of the method was not guaranteed because the time frame of the study was short.

Following the CNC machine, defect recognition and classification methods were applied in process controls such as bread manufacturing, where robots continue to be responsible for picking, packing, and palletizing [10]. The robots visually examine all the bread in the assembly line and discard the bread with unqualified shapes. The robots then pack the qualified bread and palletize it for shipping to stores.

Lately, object classification has become popular for video-based face recognition and other surveillance activities [11-13]. Bayesian network classifiers are widely used in many fields for classifying image and video data so that the image processing can be more cost-efficient. One area of the work is to reduce the parameters involved in Bayesian network classifiers [14]. Some of the other works were focused on deeply reconstructing the image/video data so that the classification can be fast and have self-studying ability [15].

2.4 References

[1] Y. Tsai, A new approach for image thresholding under uneven lighting conditions, Computer and Information Science (2007 ICIS), 6th IEEE/ACIS International Conference on, 2007.

[2] P. Kanungo, P.K. Nanda, and A. Ghosh, Parallel genetic algorithm based adaptive thresholding for image segmentation under uneven lighting conditions, *2010 IEEE conference proceeding*.

[3] T. Wu and K. Qin, Image data field for homogeneous region based segmentation, *Computers and Electrical Engineering*, Vol. 38, pp. 459-470, 2012

[4] B. Lelandais, Dealing with uncertainty and imprecision in image segmentation using belief function theory, International Journal of Approximate Reasoning, Vol. 55, Iss. 1, Part. 3, pp. 376 – 387, Jan. 2014

[5] X. Zhao, Quantification of extensional uncertainty of segmented image objects by random sets, *Geoscience and Remote Sensing, IEEE Transactions on.* Vol. 49, Iss. 7, pp. 2548 – 2557 Mar. 2011

[6] Q. Huang, W. Gao, and Wen. Cai, Thresholding technique with adaptive window selection for uneven lighting image, *Pattern Recognition Letters,* Vol. 26, pp. 801-808, 2005

[7] L. Ma and R.C. Staunton, A modified fuzzy C-means image segmentation algorithm for use with uneven illumination patterns, *Pattern Recognition,* Vol. 40, pp. 3005-3011, 2007

[8] S. Arora, Multilevel thresholding for image segmentation through a fast statistical recursive algorithm, *Pattern Recognition Letters*, Vol. 29, pp. 119-125, 2008.

[9] EN. Landis and P. Navi, Modeling crack propagation in wood and wood composites. A review COST action E35 2004 – 2008: Wood machining – micromechanics and fracture. *Holzforschung*, Vol. 63, Iss. 2, pp. 150 – 156 Aug. 2008

[10] G. Taylor and L. Kleeman, "Visual Perception and Robotic Manipulation 3D Object Recognition, Tracking and Hand-Eye Coordination" Springer Berlin / Heidelberg, 2006

[11] J. R. Barr, Face recognition from video: A review, *International Journal of Pattern Recognition and Artificial Intelligence*, Vol. 26(05), p. 1266002, Aug. 2012

[12] P. Korshunov, Video quality for face detection, recognition, and tracking, *ACM Transactions on Multimedia Computing, Communications, and Applications*, Vol. 7 (3), pp. 1-21, Aug. 2011

[13] K.N. Jae Young Choi, Face feature weighted fusion based on fuzzy membership degree for video face recognition, *IEEE Transactions on Systems, Man, and Cybernetics*, Part B, Vol. 42(4), pp. 1270 – 1282, Aug. 2012

[14] J. Hernández-González, Learning Bayesian network classifiers from label proportions, *Pattern Recognition*, Vol. 46(12), pp. 3425-3440, 2013

[15] P. H. Bartels and J. Bellamy, Self-optimizing, self-learning system in pictorial pattern recognition, *Applied optics*, Vol. 9(11), pp.2453 – 2458, Jan. 1970.

CHAPTER 3. FEASIBILITY OF AUTOMATIC DECTION OF SURFACE CRACKS IN WIND TURBINES BLADES

Huiyi Zhang, John Jackman

A paper published in the journal Wind Engineering, 2014, 38(6), pp 575-5

3.1 Abstract

Cracks on the surface of a wind turbine blade (WTB) can be a sign of current or future damage to the underlying structure depending on the severity of the cracks. We investigated a new method for automatically detecting surface cracks based on image processing techniques. The method was evaluated by varying crack parameters and parameters used in our method. Identifying and quantifying cracks as small as hair thickness is possible with this technique. Orientation of a crack did not affect the results. The effects of uneven background illumination (present in images captured on-tower) were significantly reduced by optimizing threshold value for the Canny edge detection method. The accuracy of quantifying a crack was increased by reducing noise by processing an image with both the Sobel and Canny methods and then combining the results. [1]

3.2 Introduction

Visual inspection is widely used as part of routine maintenance programs for large scale structures such as WTBs, aircraft, and bridges. Given the scale of these structures, inspection times are lengthy and the accuracy of the results depends on the skill of the inspector. Visual inspection is prone to distractions and eye fatigue [2]. For WTB inspection, inspector safety is also a concern because “sky workers” perform the inspection while suspended by a rope attached to the turbine or supported by a platform [3]. An alternative to sky workers is the use of telescopes mounted on the ground. It is well established that eye strain and eye fatigue occur in long term use of telescopes [4]. Visual inspections are not consistent because inspectors vary in their ability to detect small surface flaws that accumulate under normal blade working conditions such as hairline cracks on the blade surface.

WTBs account for 20% of the total turbine cost and pose a major challenge for maintenance due to the large-scale, on-tower location, and complex materials [5]. The annual Operation & Maintenance (O&M) cost of a wind farm is on the order of 0.5 – 2.5 cents/kWh based on the capacity and the operation years and it accounts for 10 - 20% of the total cost of energy (COE) for a wind project, based on current COE figures of 3.5 – 6 cents/kWh [6]. Although information is scarce on the cost breakdown of components in O&M, blade failure ranks in the top third of failure rates among all the critical large mechanical components. In addition, it adds a significant downtime per failure, 4 days on average, using expensive cranes and skilled technicians [7]. Early inspection can help prevent severe structural damage and reduce O&M costs (SGS Group, 2010). The SGS Group points out that repairing a blade with significant damage costs 26% of the original blade cost. If the problem is detected early enough by using a third-party inspection company, the cost would be 0.64% of the original blade cost [8].

Turbine blades generally are coated with two thin protective layers, a gel coat and a water-based varnish, to prevent infiltration of moisture, sand, and salt into the underlying fiberglass composite material which can lead to delamination and other types of structural damage. Depending on the stress applied to the blade surface, the thickness of the gel coat may vary between 0.3mm where loads are light and 0.6mm along the leading edge where it makes first contact with wind and loads are particularly high [9]. The health of the protective layers is a major O&M concern and is a significant contribution to COE using existing on-tower inspection and repair methods. Companies like BASF have made numerous efforts to develop more durable coating materials [10]. However, gel coat defects like cracks and erosion can still occur as soon as several months after starting in operation due to environment events such as heavy rains. With wind energy moving offshore, the blades will experience a more challenging environment – high moisture and salt – and potentially higher O&M costs.

Cracks that occur in the protective layers include stress cracks, crazing, and thermal cracks as shown in Figure 1. These can significantly reduce the aerodynamic efficiency of blades and lead to structural damage, which is more difficult to detect and repair. This paper addresses the characteristics of the WTB surface flaws and method parameters for automatic computer-aided optical inspection. Similar methods have been studied for aircraft health inspection. For example, a stereoscopic method has been successfully applied to a limited number of surface cracks on aircraft skins [11], [12]. The remainder of the paper is organized as follows. In the next section we describe the methodology of crack detection. Then we present the results for some candidate images, followed by concluding remarks.

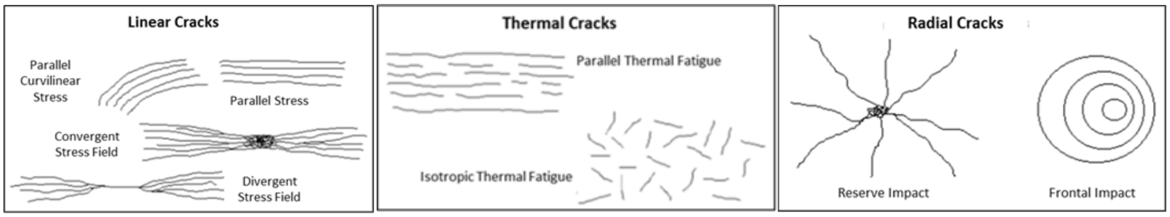

Figure 1. Types of Gel Coat Cracks.

3.3 Methodology

The three stage crack detection methodology includes: (1) a line detection method to quickly scan a WTB and locate crack regions, (2) an edge detection method that produces a detailed representation of a crack, and (3) a crack quantification method that characterizes the severity of a crack (e.g., size, color).

A series of synthetic cracks were created to control the common characteristics of surface cracks so that we could study the factors that affect the visibility of a surface defect. Brownian motion was used to create a random crack with correlation between neighboring points on the crack. Variations in thickness and color were also considered.

3.3.1 Synthetic crack generation

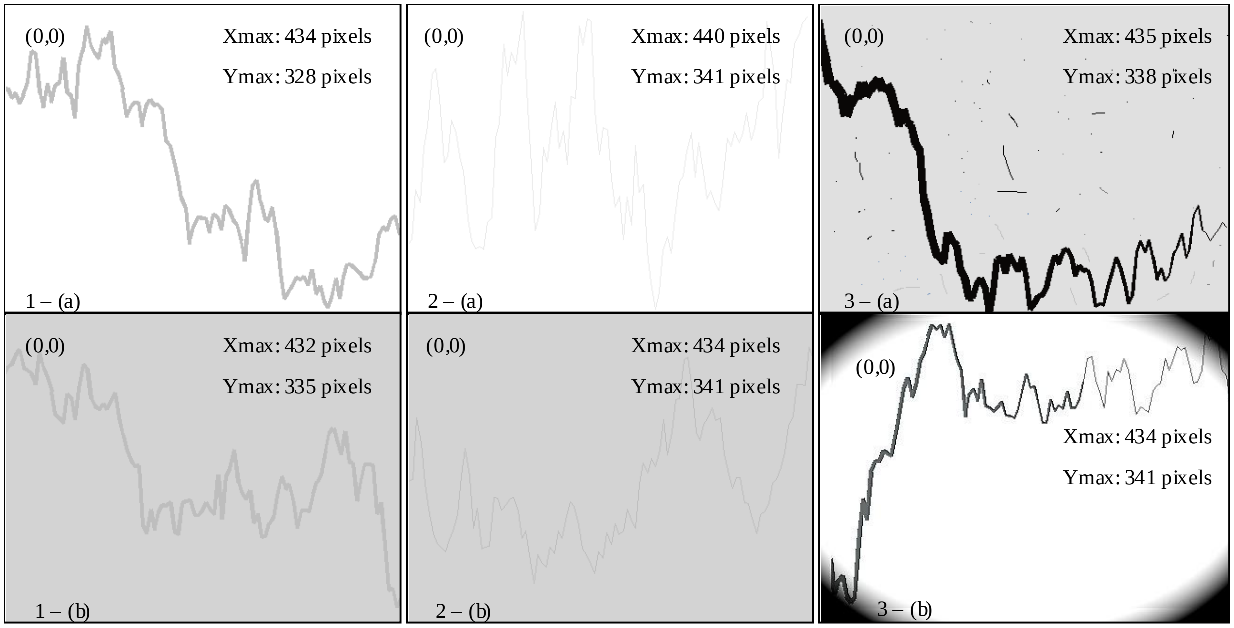

Figure 2. Synthetic cracks: 1. Different intensity level of pixels 2. Hairline thickness cracks 3. Noises & uneven illumination

A set of representative synthetic cracks was generated with one-dimensional Brownian motion in a controlled fashion as shown in Figure 2. One-dimensional Brownian motion represents a random displacement from the current location based on random number generated from a standard normal distribution. The background color of the region surrounding the synthetic cracks was defined as either white or light gray to be consistent with the paint color of a blade. The color of the synthetic crack itself was varied to represent the severity of a crack. The color of surface cracks gradually changes as the cracks go deeper into the surface and become easier to identify in digital images. The complexity of a surface crack was reflected in its non-uniform thickness, variation in color, and small deviations along the direction of crack propagation.

Differences in the intensity level of pixels, irregular distribution and geometry of noise (e.g., dirt), and uneven illumination of the image background are three major factors that can decrease the detectability of a crack [13]. The geometry and color of a crack may have some level of impact on the defect detectability. Therefore, we generated three representative groups of synthetic cracks to test the corresponding three hypotheses listed in Table 1.

Table 1. The characteristics of cracks to test the hypotheses

No.	Hypothesis	Characteristics of cracks
1	Different intensity levels of background pixels affect the detectability cracks using image processing techniques.	The color of the cracks is the same, but the background color is either white or light gray.
2	Automatic crack detection can detect small thickness cracks or weak intensity levels of pixels that an inspector would miss.	Small color differences were defined between a crack and its background. Crack thickness was set to one pixel.
3	Irregular noise and uneven illumination affect detectability of cracks.	Non-uniform thickness of two synthetic crack images. One has irregular noise and the other has uneven illumination.

Three field images were selected to further investigate the hypotheses in Table 1 and to evaluate if the parameters that define the detectability are consistent with the six synthetic cracks. After testing the method on the three groups of synthetic cracks, the field images shown in Figure 3 were used to evaluate the accuracy of the method. The results were compared to the synthetic cracks to check whether the synthetic cracks captured the basic characteristics of real cracks.

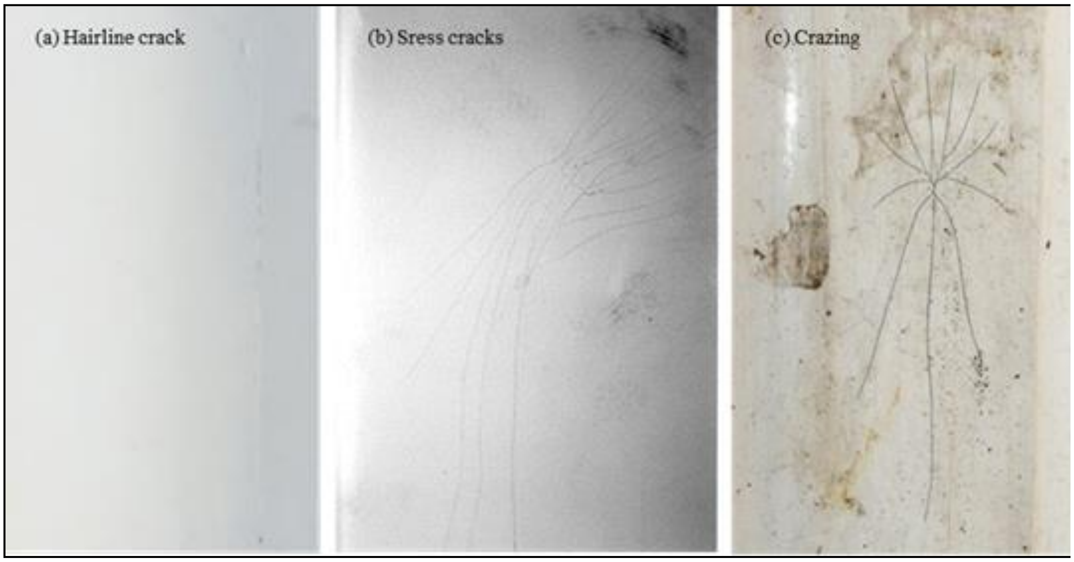

Figure 3. (a) Hairline crack (RGB image: 157-by-272). (b) Stress cracks (Gray-scale: 247-by-350). (c) Crazing (RGB image: 270-by-435).

One of the field images in Figure 3 (a) was a hairline crack and is the most difficult flaw to detect with the human eye. The hairline cracks shared the same characteristics as the synthetic cracks in the second group as shown in Figure 2-2 (a) and (b) . The second image was a stress crack as shown in Figure 3 (b). It was used to investigate the effect (if any) of uneven illumination on the detectability of an image. It was also used to assess the importance of the direction of the line detection masks. The third crack as shown in Figure 3 (c) was crazing, which typically has a spider web geometry and some of the small cracks in a crazing may not coincide with the four directions of standard line detection masks. The images in Figure 3 (b) and (c) were used to evaluate the effects of uneven illumination and noise on the detectability of cracks, corresponding to the synthetic cracks in group three as shown in Figure 2-3 (a) and (b). The background color of Figure 3 (a) and (b) was light gray and Figure 3 (c) had a white background color, which corresponds to the synthetic cracks in the first group of Table 1.

3.3.2 Line detection

A line detection method was used to perform a quick scan on a blade. It is simple, fast, and sensitive to individual line segments. Cracks can be treated as a set of connected segments. A line is a basic type of intensity discontinuity in a digital image and the most common method to detect them is to process the image with a linear spatial filter mask having a binary format. The process consists of moving the center of the mask to each pixel in an image and computing the response at each pixel, which is the sum of the product of the mask coefficients and the intensity of the 8 neighboring pixels and is given by

$$\mathrm{R} = \sum_{\mathrm{i}=1}^{8} \mathrm{w_i z_i} \qquad (1)$$

where, $\mathrm{z_i}$ is the intensity of the pixel associated with the mask coefficient $\mathrm{w_i}$.

Theoretically, only an odd number size of the mask is considered since R is the response from the center of the filter mask at a specific pixel, $(\mathrm{x, y})$. The smallest mask is a 3×3 matrix (i.e., 8 neighboring pixels). There are four standard line detection masks corresponding to the orientation of the lines, namely, horizontal, 45˚, vertical, and -45˚ as shown in Table 2. The larger number – 2 – in the mask matrix represents the direction of the mask and it has a strong response to one pixel thickness segments. Increasing the number from 2 to 3 will smooth the output image but continually increasing the number will create fuzzy results. Although the vertical line detector masks responded strongly to one pixel thickness lines, it can also detect vertical lines with different thicknesses. A binary union operation between the four standard line detector masks creates a composite mask that can detect lines in any direction.

A threshold value was used to convert a gray-scale image to a binary image. Suppose $\mathrm{f(x, y)}$ represents the intensity of a pixel at $\mathrm{(x, y)}$ and T is a selected threshold value, any pixel where $\mathrm{f(x, y) \geq T}$ is set to 1 and is classified as an object pixel. Otherwise, the pixel is set to 0 and is classified as a background pixel. A threshold image $\mathrm{g(x, y)}$ is defined as

$$\mathrm{g(x, y)} = \begin{cases} 1 \text{ if } \mathrm{f(x, y) \geq T} \\ 0 \text{ if } \mathrm{f(x, y) < T} \end{cases} \tag{2}$$

Table 2. Standard line detector masks

-1	-1	-1
2	2	2
-1	-1	-1

(a) Horizontal.

2	-1	-1
-1	2	-1
-1	-1	2

(b) 45°.

-1	2	-1
-1	2	-1
-1	2	-1

(c) Vertical.

-1	-1	2
-1	2	-1
2	-1	-1

(d) -45°

The MATLAB toolbox provides a function, graythresh, that computes a threshold using Ostu’s method [13]. However, this method tends to generate significant noise when the background illumination is uneven.

3.3.3 Edge detection

A major advantage of edge detection is that uneven illumination does not affect the detectability of an edge. Edge detection was used to capture the outer contour of non-uniform thickness cracks and to complement the inadequacy of line detectors in detecting meaningful discontinuities in intensity values. Unlike line detection, edge detection uses first- or second-order derivatives to compute the maximum rate of change of grayscale levels of pixels. Edge detection gave much smoother results by eliminating noise with a small number of pixels. However, this process may take a long time when the size of the images are large like 2 MB per image. Therefore, line detection was applied first so that a fast scan of the entire blade can be performed in a reasonable amount of time and then the edge detection method was used to extract smoothing information from the areas identified by the line detection.

The MATLAB function, edge(), supports several common detection methods including: Sobel, Prewitt, Laplacian of a Gaussian (LoG), and Canny. The key difference between these methods is how the first or second-order derivatives are approximated. The first order derivative in image processing is a vector for a 2D function $\mathrm{f(x, y)}$ given by

$$\nabla \mathrm{f} = \begin{bmatrix} \mathrm{G_x} \\ \mathrm{G_y} \end{bmatrix} = \begin{bmatrix} \frac{\partial \mathrm{f}}{\partial \mathrm{x}} \\ \frac{\partial \mathrm{f}}{\partial \mathrm{y}} \end{bmatrix} \tag{3}$$

with the magnitude of the vector being $\mathrm{g} = \mathrm{mag}(\nabla \mathrm{f}) = \left[\mathrm{G_x^2} + \mathrm{G_y^2}\right]^{1/2}$ and the angle is $\alpha(\mathrm{x, y}) = \tan^{-1}(\frac{\mathrm{G_x}}{\mathrm{G_y}})$, where the angle defines the edge direction. Both Sobel and Canny methods were considered since Sobel is the most commonly used and Canny is considered to be the most powerful edge detector. The Sobel method had default masks as shown in Table 3 to compute the gradient, $\nabla \mathrm{f}$, which is composed of vectors $\mathrm{G_x}$ and $\mathrm{G_y}$, given by

$$\mathrm{G_x} = (\mathrm{z_7} + 2\mathrm{z_8} + \mathrm{z_9}) - (\mathrm{z_1} + 2\mathrm{z_2} + \mathrm{z_3}) \text{ and}$$

$$\mathrm{G_y} = (\mathrm{z_3} + 2\mathrm{z_6} + \mathrm{z_9}) - (\mathrm{z_1} + 2\mathrm{z_4} + \mathrm{z_7}). \tag{4}$$

where $\mathrm{z_1, \ldots, z_9}$ are the pixel values in the image that span the Sobel masks.

Table 3. Sobel detector masks.

-1	-2	-1
0	0	0

-1	0	1
-2	0	2

1	2	1

(a)

Vertical.

-1	0	1

(b)

Horizontal.

The Canny method is more complex and includes a Gaussian filter, a local gradient, an edge direction computation algorithm, and provides edge linking by incorporating the weak pixels that are connected to the strong pixels.

The default threshold number for the Sobel and Canny methods does not guarantee a positive result. However, both of these methods offer promising results by optimizing the threshold value. The Sobel method offered less noisy results as compared to the Canny method but also tended to miss a significant number of the defects. By updating the threshold number, the Canny method produced the smoothest result. The Sobel method did not reduce the background noise significantly as the threshold value was adjusted. On the other side, the noise generated by Sobel operator looks like points, where Canny's noise tended to be small segments. If we treat the noisy results as connected pixels, then we can filter them by eliminating number of connected pixels less than a specific number, say 3 pixels. With this method, Sobel operator can eliminate noisy results better because the noise results generated by sobel operator are small dots.

Adjustment of threshold number required a lot of human intervention, which is not the goal of this research. The default threshold value was used as a starting point and was adjusted using a fixed step size. The edge detection method was performed with the new threshold value and the results were compared with the previous results to determine if the difference is within an acceptable tolerance. For example, the default threshold value for the Canny method is $\mathrm{T} = [\mathrm{t}_1, \mathrm{t}_2]$ that produces a matrix A_0 containing all the detected edges corresponding to the cracks. The threshold value was updated to $\mathrm{T}_1 = [\mathrm{t}_1 + .1 \times (\mathrm{t}_2 - \mathrm{t}_1), \mathrm{t}_2 - .1 \times (\mathrm{t}_2 - \mathrm{t}_1)]$ and applied again, producing a new set of detected edges in matrix $\mathrm{A_1}$. The process was repeated until $\mathrm{A_{i+1} - A_i} \leq \mathrm{D}$, where D is standard deviation of all As.

3.3.4 Quantifying crack severity

Two methods were used to quantify the severity of a crack. The easiest method is to find the bounding rectangle (parallel to the x and y axes) that encloses the pixels from the edge detection method. This region identifies the most likely required repair area. However, it did not provide any further information about the orientation of the crack and tended to overestimate the magnitude.

The second approach was to find the minimum envelope that encloses the crack (i.e., the envelope orientation is not constrained). The envelope can be found by estimating the parameters of a line that minimizes the maximum distance to all the points on the crack edges. Using the start and end points of the detected edges, the sides of the envelope can be found by projecting the end points onto the estimated line. The other two sides of the envelope correspond to the maximum deviation of the crack on each side of the line.

To minimize the maximum distance to the line, the function fminimax in MATLAB was used to find the best fit parametric line, denoted by $\begin{cases} \mathrm{x=at+b} \\ \mathrm{y=ct+d} \end{cases}$. The function, fminimax, requires an initial guess for the parameters of the line [a, b, c, d] and a function that computes the maximum distance of all points along the edges to the given line. The function stops when the values of [a, b, c, d] are within a specified tolerance (i.e., the change is negligible) or a maximum number of iterations is reached. The default iteration limit is 500 in MATLAB. In this study a limit of 2500 iterations was used.

3.3.5 Potential errors

Any inspection technique can result in two kinds of errors: false-positive (Type 1) or a defect is missed (Type 2). For crack detection, a Type 1 error can be caused by noise, which cannot be totally avoided. Missing a defect (Type 2) could occur due to uneven illumination or line and edge detection method parameters. The consequences of a Type 1 error in this context are not as severe as the Type 2 error, since missing defects can lead to ignoring the necessary maintenance, leading to future structural damage. Type 2 error can be reduced significantly by adjusting the threshold values.

3.4 Results

The results of the image processing show that (1) noise, intensity level of pixels, and uneven illumination are major factors that affect detectability, (2) the line detection method is capable of quickly scanning a blade to find crack regions, and (3) uneven illumination is not a major factor in edge detection methods. The Canny method offers the best results in detecting discontinuities in the surface. The severity of a crack is difficult to quantify because we only considered 2D images in the paper. However, the crack size and intensity level of pixels offer important insights on the magnitude of a crack.

The six synthetic cracks and three representative field images were tested with both line and edge detection methods. The Canny method had the best results by far in terms of detecting discontinuities in the surface. Generally, uneven illumination had much less influence on the detectability of edge detection methods as compared to line detection. For a very bright background, edge detection offered much better results. Unlike line detection, edge detection eliminated low levels of noise and the detected edges were much smoother.

3.4.1 Factors affecting detectability

The intensity level of pixels is important. The results for the first group of synthetic cracks did not indicate that our method can detect a crack with a lighter background color easier than an image with a darker background color. When applying the MATLAB graythresh function, the two images resulted in very different optimal threshold numbers and both of the images resulted in clearly delineated defects. Not surprisingly, the applicable threshold range was significantly different for the two images. The one with a white background had an acceptable threshold value from 0.746 to 0.999. The image with a gray background had an acceptable threshold value between 0.745 and 0.827. Higher threshold values eliminated more noise with low- to middle-level intensity levels for pixels in the background, which can make the results more definitive if there is a lot of noise in the background. However, the tradeoff is that some of the defects will be filtered out if the defect has a lower intensity level than the noise in the background.

Surprisingly, crack thickness did not affect the detectability of a crack for synthetic cracks and field images. Also, crack orientation was not a significant factor. In the line detection method, when images were rotated counter-clockwise in 10 degree increments, the line detector masks were able to detect lines all directions. Edge detection methods are based on first- or second-order derivatives, which are not affected by crack orientation. Therefore, both line and edge detection methods were not affected by crack orientation. In other words, the orientation of the field camera is not expected to affect the results. These results suggest that the computer-based method may be a better alternative to using sky workers for visual inspection of blade surfaces.

Background illumination is important because automatic threshold computing methods tend to fail when the background illumination of an image is uneven (i.e., there is variance in the pixel values). Uneven illumination had a severe impact on the line detection method as shown in

Figure 4(b). The original image of stress cracks in Figure 3(b) had very bright lighting on the background and the results were poor. Therefore, the lighting problem still poses a challenge to line detection. This problem can be addressed to a limited extent with existing image processing techniques. Further research is warranted to reduce the effects of uneven lighting on crack detection. Edge detection methods reduce the uneven illumination problem for the same cracks as shown in Figure 5 (b) and (d). Also edge detection methods reduce the background noise problem for the crazing cracks shown in Figure 6. This supports the hypothesis we made earlier that it would be most effective to use the line detection method to perform a quick scan and then apply an edge detection method to investigate the details of a crack.

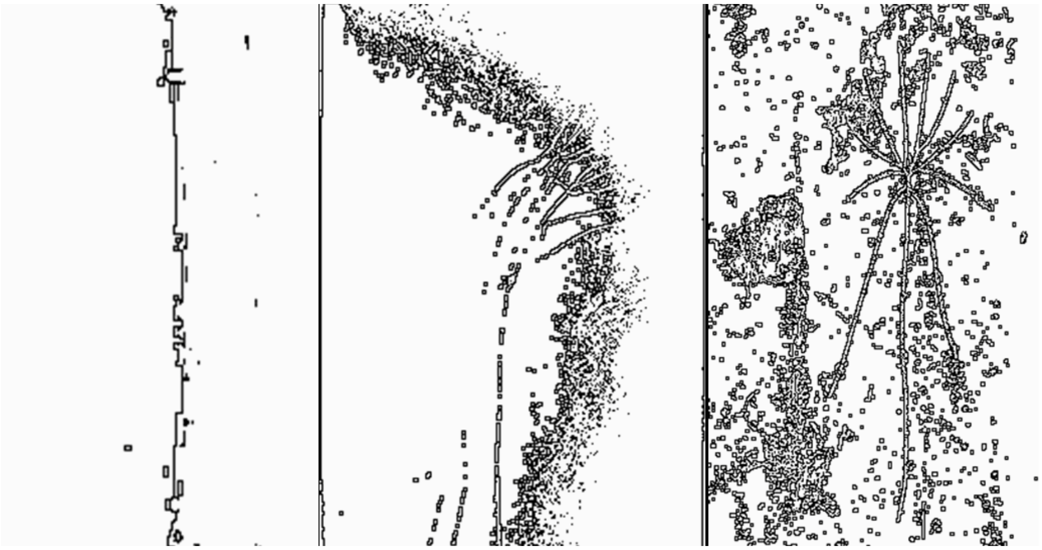

(a) Hairline crack. (b) Stress cracks. (c) Crazing.

Figure 4. Field sample of edge detection for detailed defects

3.4.2 Edge detection

Edge detection methods like Sobel and Canny produced much smoother results than the line detection method. Noise and uneven illumination did not have a significant impact on edge detection. The intensity level of pixels is very important to both line and edge detection methods because if the intensity level of noise is larger than the intensity level of the defect, the defect will not be detected since the method will consider it to be background noise and eliminate it.

When testing synthetic cracks with the line and edge detection methods, the first two groups or the first four synthetic cracks had the same results. Neither the color or size of the crack affected the result. In other words, both the line and edge detection methods could easily detect hairline cracks when there is no significant background noise or no uneven illuminations. However, both the Sobel and Canny methods required adjustments to the threshold values to detect some cracks. Without these adjustments, these methods had difficulty detecting stress cracks with under uneven illumination conditions and crazing cracks with noisy backgrounds.

With the default threshold value, Canny operator offered much better results as shown in Figure 5 (c), where sobel method had too much Type 2 error as shown in Figure 5 (a). Both sobel and Canny operators could produce better results by optimizing the threshold values as shown in Figure 5 (b) and (d). However, the Canny result is much smoother but its noisy results is also much stronger as shown in Figure 5 (d).

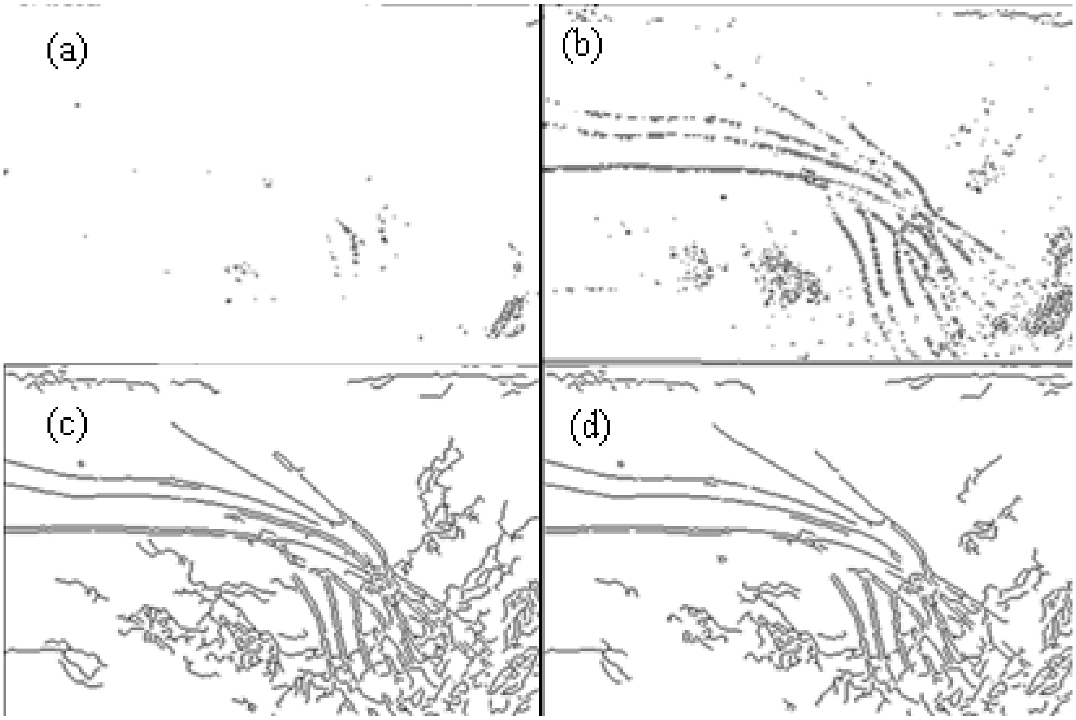

(a) *Sobel* operator with default threshold (b) Sobel operator with optimal
threshold
(c) *Canny* operator with default threshold (d) *Canny* operator with optimal

The crazing crack from Figure 5(c) contains a lot of noise, which is common to blades. Both the Canny and Sobel methods were able to reduce the background noise effect, which means the computer-based optical inspection method is feasible for on-site application. See Figure 6.

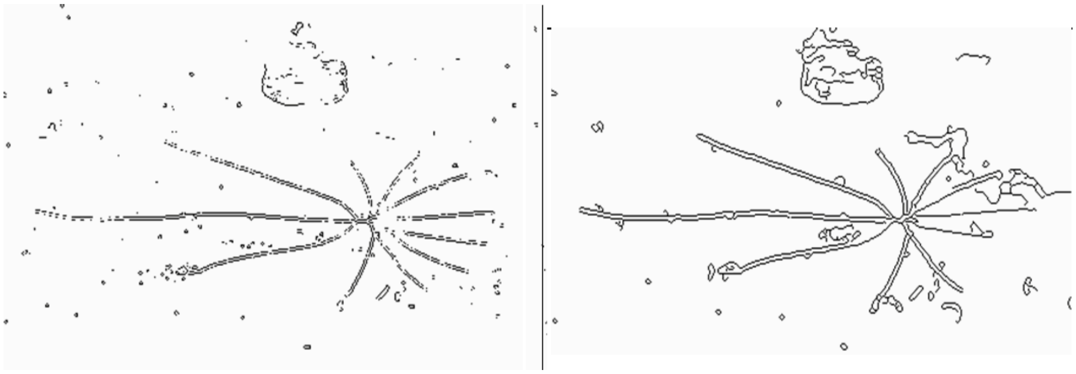

(a) *Sobel* operator (b) *Canny* operator
Figure 6. Edge detection reduce noise significantly

3.4.3 Quantifying the cracks

After the cracks were detected, they were bounded in a rectangle and a minimum enclosing envelope. The rectangle indicated the recommended repair area. The envelope provided additional information on the direction and magnitude of the cracks. However, if there was a lot of noise, the parallel lines were just the lines parallel to a line with minimized maximum distance to all the points detected, which included noisy results and very small flaws as seen in the results in Figure 4(c). Therefore, eliminating noise as much as possible is very important in estimating the magnitude of a crack.

The first synthetic crack in Group 1 was selected to address the capability of quantifying a crack since the direction of the crack is clear and it is easy to determine if the approximation line follows the direction of the crack. First, the recommended repair area is enclosed in the yellow rectangle with 423-by-301 pixels as shown in Figure 7, where the original image has 434-by-328 pixels shown in Figure 2-1(a). The minimum envelope for the crack was bounded by the light blue lines that are parallel to the purple line with parametric equations listed below.

$$\begin{cases} \mathrm{x} = 439.2590 * \mathrm{t} + 202.6571 \\ \mathrm{y} = 277.2023 * \mathrm{t} + 166.7593 \end{cases} \tag{5}$$

where $\mathrm{t} \in [-0.46, 0.502]$.

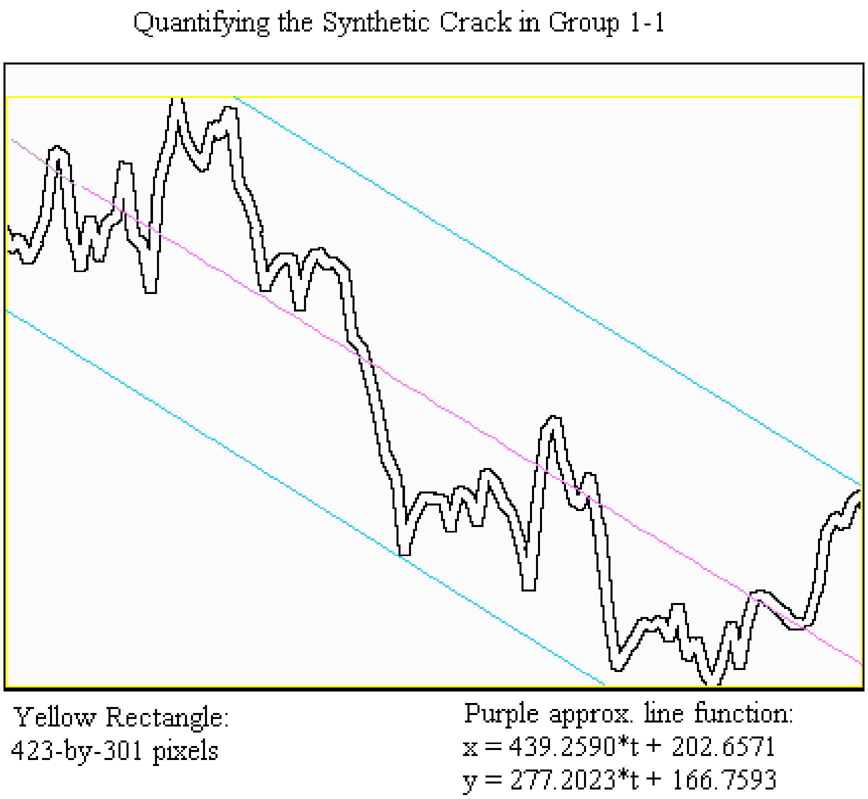

Figure 7. Quantification of the Synthetic Crack in Figure 2-1- (a)

The two parallel lines in light blue enclosed the cracks with minimum distance to the purple line as shown in Figure 7. The severity of a crack was defined by its intensity along the crack. The location of the cracks on the blade can be critical. For instance, if a crack occurred along the leading edge or the root section, it may create greater damage or accelerate structural damage than in other areas since the leading edge contacts the wind first and the root section is affected by a greater accumulation of fatigue loads.

3.4.4 More field images

A set of 27 field images were collected at Fraunhofer-IWES in Aug. 2013. The 27 images were processed with the edge detection methods and the results were consistent. One of the sample cracks were detected and quantified as shown in Figure 8.

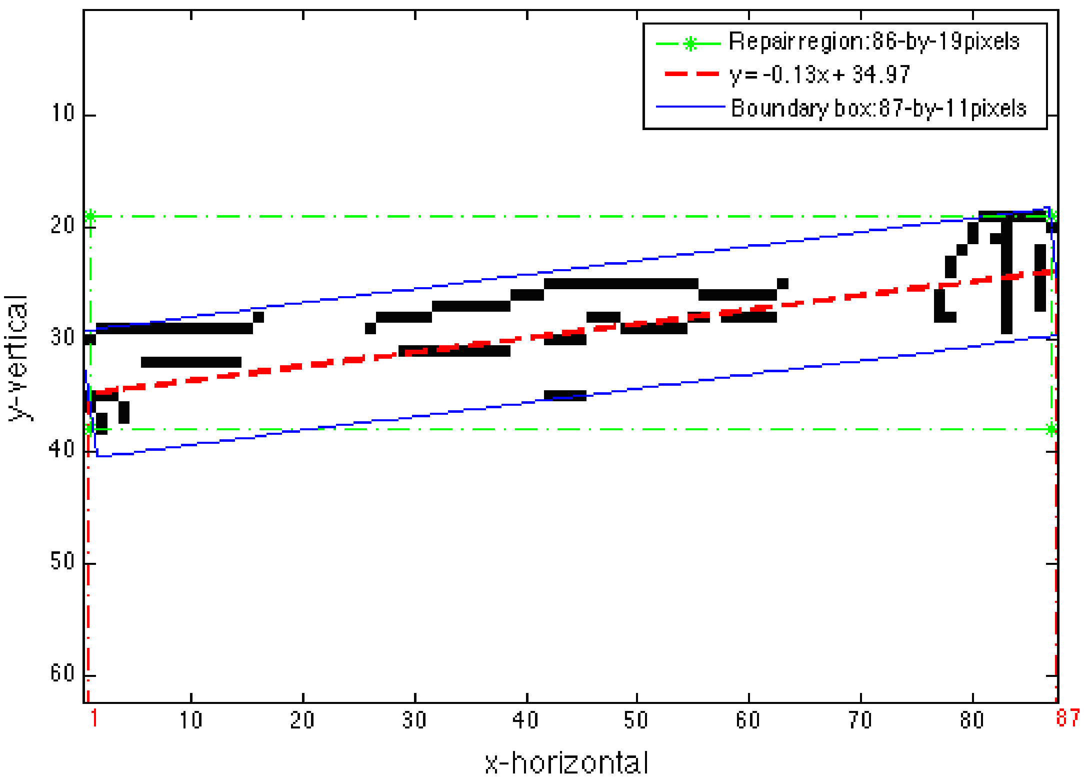

Figure 8. Quantification of a field image with a crack

3.5 Conclusion and future work

This paper evaluated two image processing techniques for detecting cracks in wind turbine blades, namely, the line detection method and the edge method. The original hypothesis was that the line detection method would be best for performing a quick scan of the blade surface to find crack regions and that the edge method would provide a more detailed description of cracks. The results of the study support this hypothesis.

The line detection method is appropriate for quick scans because it can quickly identify hairline cracks that are invisible to the naked eye. Image processing thresholds and filters can be used to minimize false-positives caused by surface irregularities like dirt or dust. However, uneven illumination poses serious problems for the line detection method that cannot be overcome.

The edge detection method provides more detailed information about cracks than line detection, but is so detailed that it has difficulty distinguishing between surface irregularities and cracks. The most effective method we recommend is to first identify crack regions using the line detection method followed by edge detection to collect more information on the cracks. Edge detection is particularly useful when there is uneven illumination.

The results showed that automated optical inspection for crack detection shows promise for maintenance work on in-service wind turbine blades. With a high quality image and processing tools, image processing techniques can consistently identify cracks that are invisible to human eyes, even when looking at the blade from different angles. Further research is necessary to apply these methods to more sample cracks and to investigate methods that minimize errors caused by uneven lighting.

3.6 References

[1] Zhang, H. and Jackman, J. A feasibility study of wind turbine blade surface crack detection using an optical inspection method, Renewable Energy Research and Applications (ICRERA), 2013 International Conference on, published in 2013, pp. 847-852, DOI: 10.1109/ICRERA.2013.6749869

[2] Trimm, M. An overview of nondestructive evaluation methods. Practical Failure Analysis 3.3 (2003): 17-31.

[3] Marsh, G. Meeting the challenge of wind turbine blade repair. Reinforced Plastics, July-August, 2011, Vol.55(4), p.32(5)

[4] Hanson, R. J. E. Visual fatigue and eye strain in the use of telescopes. Transactions of the Optical Society 22.1 (1920): 26.

[5] Hutchinson, J.R., Schubel, P.J., and Warrior, N.A., A cost and performance comparison of LRTM and VI for the manufacture of large scale wind turbine blades, Renewable Energy, 36 (2011) pp. 866-871

[6] Walford, Christopher A. Wind turbine reliability: Understanding and minimizing wind turbine operation and maintenance costs Global Energy Concepts, LLC. Sandia Report: SAND2006-1100 Mar. 2006.

[7] Hahn, B. (1999). "Reliability Assessment of Wind Turbines in Germany." 1999 European Wind Energy Conference, Nice, France, March 1-5.

[8] SGS Group, The cost of wind blade inspections versus blade repair. Hamburg, Germany, available on-line at http://www.nacleanenergy.com/oldsite/index.php?option=com_content&view=article&id=2327:the-cost-of-wind-blade-inspections-versus-blade-repair&catid=42:feature-articles&Itemid=109

[9] ABB robotics. "ABB Robotics – Painting wind turbine rotor blades." Dec., 2009, available on-line at http://robotize.com.au/roboticnews/videos/25ba98/ABB-Robotics-Painting-wind-turbine-rotor-blades/

[10] BASF, "Chemistry makes wind power more economic.", "New epoxy resin for high-performance rotor blades.", and "Special protective coating increases the profitability of wind turbine systems." Aug. 2014, Available on-line at http://www.basf.com/group/corporate/en/sustainability/environment/climate-protection/solutions/energy.

[11] Siegel, M., Enhanced remote visual inspection of aircraft skin. Robot Institute. Carnegie Mellon University. Proceedings of the Intelligent NDE Sciences for Aging and Futuristic Aircraft Workshop, September, 1997, pp. 101 - 112.

[12] Giakoumis, L., Digital Image Processing Techniques for the Detection and Removal of Cracks in Digitized Paintings IEEE Transaction on Image Processing, Vol. 15, No. 1, January 2006

[13] Gonzalez, Rafael C. Digital Image Using MATLAB Processing. Upper Saddle River, New Jersey, 2004, Pearson Education, Inc.

CHAPTER 4. IMAGE SEGMENTATION AND LINKAGE TECHNIQUES TO DETECT GEL COAT CRACKS WITH SEVERE BACKGROUND NOISE

A paper to be submitted to IEEE Transaction on Image Processing

4.1 Abstract

Visual inspection plays a vital role in routine health inspection of wind turbine blades (WTBs), where on tower practice brings uncertainty to the inspection results as well as safety concerns of the site employees. This paper proposes a threshold-based method to continuously detect cracks along the blade surface coating with severe background noise and uneven illumination, which can be applied to future automatic inspection devices. The paper classifies the types of surface defects based on previous studies and on-site experience. A pattern recognition method was applied to compute the threshold value for edge detection with a *sobel* operator. Flood fill algorithm was used to extract connected components from a single image and a histogram of connected components was applied to determine the "best-fit" threshold value for removing background noise like dust and insects that pass through edge detection. Finally, edge linking techniques were modified to fill gaps within a crack and determine its branches.

4.2 Introduction

Structural health monitoring is an essential component of maintaining large-scale structures such as wind turbines, aircraft, and bridges. Large composite structures (such as those found in wind turbine blades) are regularly inspected using optical methods to detect damage at an early stage. If damage is detected, additional nondestructive evaluation techniques can be used to characterize the damage [1]. Optical inspection plays an important role in reducing operation and maintenance (O&M) costs and maximizing energy production in wind farms. Blades are critical components of a wind turbine that need to be inspected regularly to decide when corrective action is warranted due to damage (such as, crack or erosion) [2], [3].

Blades are typically made of fiber-reinforced composite materials and coated with an epoxy-based gel coat layer and a waterproof paint to protect the composite structure from extended outdoor exposure. Damage can occur after production, during transportation, installation, and operation. Surface flaws as small as hairline thickness cracks allow moisture and salt in the air to penetrate the laminate structure and can lead to severe structural damage. In addition, surface roughness caused by defects will reduce the power-generating rate and can upset the balance of loads between the three blades in a typical horizontal turbine configuration [4].

Early defects within the gel coat layer tend to have low intensity color contrast with respect to the background, while environmental noise such as dust and insects have a significantly higher intensity contrast. The challenge is to identify the defects in blade images when such noise occurs. In addition, defects like cracks may have gaps, and noise makes it more difficult to recognize these gaps. Understanding the nature of defects and noise is critical to minimizing Type 1 and Type 2 errors during image processing. A Type 1 error is a false alarm (e.g., a crack was detected but there is no crack) and Type 2 error is a failure to detect an existing crack [5].

This paper describes a new crack detection technique that can identify and quantify multiple cracks from a single image with severe background noise as well as link cracks with gaps. The remainder of the article is organized as follows. In section 2, we describe the nature of blade surface defects. Section 3 explains existing and our proposed surface inspection methods as well as some of the challenges of applying image processing to blade inspection. In section 4, the methodology is described. Section 5 presents the results from analyzing sample field images using the proposed methods.

4.3 Nature of blade surface defects

Previous studies have defined the types of defects on a blade surface as the "formation and growth of cracks in the gel coat and debonding of the gel coat from the skin (gel coat cracking and gel coat/skin debonding)" [6]. The majority of cracks observed during load testing occur in the region between the root section and 2/3 of the blade length as shown in Fig. 1. While erosion can occur at any location on the leading edge, it is typically found in the tip region because of the higher speeds.

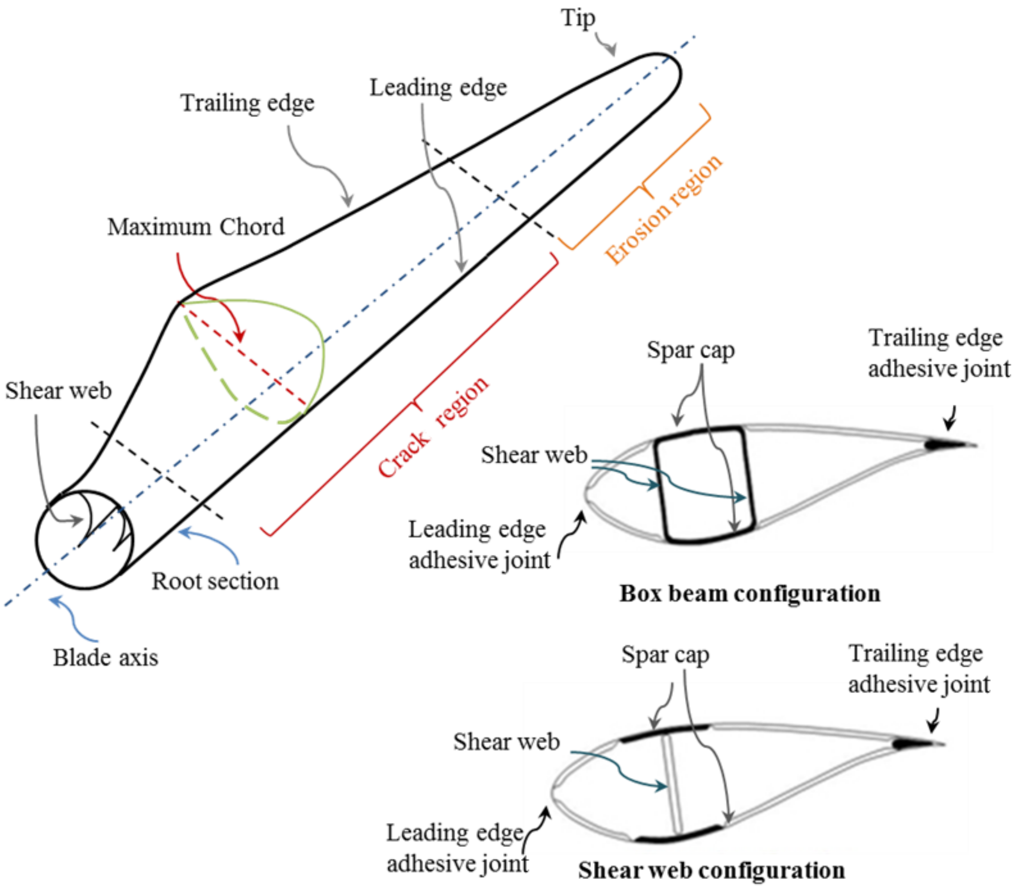

Fig. 1. Schematic of a wind turbine blade. Box beam configuration has double shear webs and is common for blades longer than 40 m. Shear web configuration has one shear web forming an I-beam with spar caps.

Based on on-site inspections by maintenance companies, surface defects can be classified as gel coat cracks, mechanical cracks, erosion, and adhesive joint failure along the leading and/or trailing edges as shown in Fig. 2.

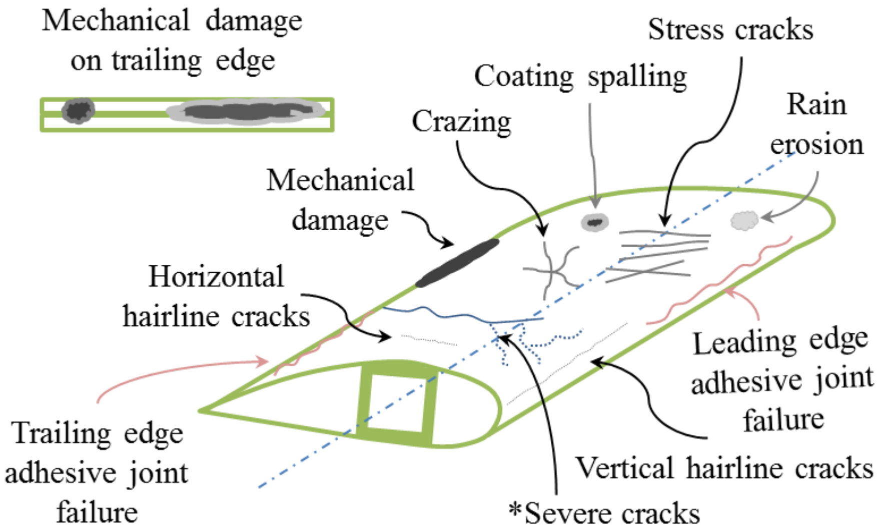

Fig. 2. Types of surface defects. Adhesive joint failure and delamination are structural failures under the surface. Severe cracks appear as horizontal cracks starting from the trailing edge that can be delamination or fiber splitting (±45º) under the coating layers [6].

4.3.1 Gel coat cracks

A gel coat layer is applied to the blade surface to increase durability by preventing ultraviolet degradation and hydrolysis. Cracks are one of the common early gel coat failures, which can be classified into three sub-categories.

- Type 1: hairline cracks – such cracks are as small as hairline thickness and are difficult to see with the human eye. These cracks occur primarily along the leading edge, but can also appear on other areas of the blade [6]. Vertical hairline cracks along the leading edge and parallel to blade axis as shown in Fig. 2 may indicate adhesive joint failure.
- Type 2: stress cracks – appear as a set of parallel or intersect lines, where the fiber laminations are under high fatigue loads and delamination has probability occurred under the gel coat. Stress cracks can occur at all points along the blade and appear most frequently

near the root section [6].

- Type 3: crazing – appears as a spider web or radial pattern. Crazing combined with a single crack near the blade tip can indicate lightning damage under the surface coating, which is generally located near the lightning protection devices along the spar cap.

4.3.2 Mechanical damage

Mechanical damage usually occurs on or near the trailing edge as shown in Fig. 2. This is because the trailing edge has a sharp transaction from the root section of the blade to the blade body, where blade has its maximum chord. Also the contact area of the trailing edge is much smaller than other parts of the blade so that if applied same force to the trailing edge, it will result much higher pressure and easy cause damage. The cause of mechanical damage can be collisions with other objects during transportation, installation, and maintenance. In addition, some severe cracks as deep as the inner laminations are usually located near the maximum aerodynamic chord with growth direction towards the leading edge and perpendicular to the blade axis. The primary cause of these cracks is that the blade design increases fatigue load at the airfoil with the maximum chord as marked in Fig. 1. It is not clearly if these cracks have directly relation to mechanical damage. Mechanical damage occurs not only on the surface coating, but may also extend into the lamination.

4.3.3 Erosion

Erosion can be classified as early gel coat erosion or spalling of the coating, which depends on how much of the coating material was removed and/or the depth of the erosion. Early gel coat erosion appears as surface material that has been removed within the gel coat layer, but has not affected the fiber lamination. Spalling is a more severe erosion of the gel coat in which the underlying fiberglass is exposed to the air. Erosion is observed primarily along the leading edge in the tip region where the blade velocity is the highest. Wind-driven raindrops are the primary cause of leading edge gel coat erosion. Rain erosion adds surface roughness, and significantly reduces the durability of coating materials and the aerodynamic performance of the blade.

4.3.4 Adhesive joint failure

Blades are often manufactured by building two half-blade shells in a pair of molds and then bonding the two halves with adhesives. The leading and trailing edges of the blade are typically along the bond lines. Manufacturing defects such as insufficient adhesive, voids, and embedded air bubbles in the bond joint contribute to debonding of the joints that appears as a severe crack along the trailing edge or may start with a hairline crack pattern along the leading edge.

4.4 Related Work

4.4.1 Remote sensor-based monitoring

Embedded fiber optic sensors have been studied to monitor turbine blade health conditions in real-time [7], [8]. These methods can generate a 3-dimensional real-time strain map, which measures the deformation of blade materials caused by the compressive force generated from wind loads. These sensors are installed in predicted critical areas of the blades, such as the spar cap. Because of the significant instrumentation costs per turbine and the difficulty to distinguish flaws from noise signals, they are not considered to be a feasible monitoring solution and are used primarily in the laboratory or at a field test site.

Acoustic emission techniques use piezoelectric sensors mounted on blade surfaces to detect blade damage and its location [9], [10]. However, this approach requires an extensive sensor network on each blade and has not been deployed because of implementation difficulties and costs.

4.4.2 Visual Inspection

Currently, routine blade health inspection is conducted by land-based telescope or on-tower inspections conducted by sky workers and/or platform-supported sky workers using visual and ultrasonic inspection techniques. Sky workers are trained to traverse a blade using a platform or a rope attached to the nacelle. Inspections and maintenance are performed along a blade's outer surface with handheld devices such as an ultrasound scanner. This method introduces significant variability in the results due to the variation in the abilities of sky workers [11].

Computer-based surface crack inspection has been investigated for routine health inspections of aircraft and a limited library of defect images has been developed [12]. A robotic inspection system consisting of digital cameras that collect high-resolution bitmaps of the surface, a complex lighting system to control illumination of the surface, and image processing techniques was used to quantify defects on aircraft surfaces [13]. However, this approach cannot be easily extended to blade surface inspection because 1) blades have more background noise like dust and insects that cannot be easily distinguished from targeted defects, 2) modern blades can be twice as large as the largest aircraft wing and therefore, the image processing speed is more critical, and 3) on-tower inspection is more challenging as compared to on-ground/in-hangar inspection of aircraft because of uncontrolled lighting.

4.4.2.1 Image Processing Techniques

Digital image processing techniques are necessary to analyze images obtained using any automated optical inspection system. Image processing can identify defects as small as one pixel and when pixel light intensities are not detectable by the human eye. However, other factors create analysis problems such as variation in image quality resulting from the image acquisition (e.g., image distortion) [14]. One particularly challenging region on the blade is to detect gel coat cracks on the trailing edge joint, which has the smallest thickness and the sharpest transition from the root section to the body section at the maximum chord as shown in Fig.1.

4.4.2.2 Image Segmentation

Image segmentation partitions an image into multiple regions to identify objects or extract other relevant information from digital images. It has been one of the most important and challenging topics in image analysis [15], [16]. Most of existing image segmentation methods are either feature extraction or feature-based segmentation. Feature extraction characterizes the homogeneity of regions in an image while feature-based segmentation assigns each pixel a label and determines which object it belongs to [17].

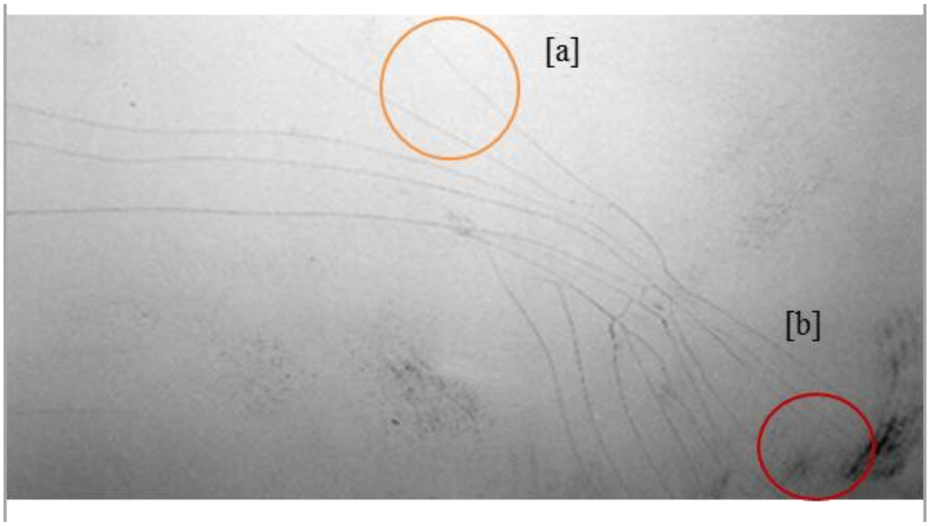

Fig. 3. Stress cracks from a field image of a blade, where region [a] has uneven illumination and region [b] has background noise [20].

Otsu’s method, also referred to as the maximization of interclass variance method, is based on the concept of thresholding segmentation [18]. A threshold value is found by maximizing the between-class variance in a grayscale image based on the distribution of pixel intensities. Pixels with intensities below the threshold value are converted to the background color and the others are considered to be useful information. Although Otsu’s method tends to fail when there is significant background noise or uneven illumination, as in Fig. 3, thresholding segmentation is still one of the most popular methods as compared to feature extraction because it saves computational time and memory usage by operating on grayscale data, and it is not limited by the number of defined features such as statistical features, frequency-domain features, and model-based features in feature extraction [19].

4.5 Methodology

The edge detection problems that need to be addressed for blade surfaces are (1) minimization of the effects of significant background noise and uneven lighting and (2) filling the gaps in cracks caused by threshold-based image processing. We introduce a new threshold for connected components to address the noise problems associated with edge detection in the context of wind turbine blades. Background noise such as insects and dirt are identified as defects using edge detection because of their high intensity contrast with the background color. This type of noise appears as single pixel or small connected components, which we filter out based on a size threshold. We named it the cc-threshold in the paper. After edge detection methods are applied, gel coat cracks are often discontinuous because of gaps created by thresholding techniques. These small discontinuities can be resolved using our edge linkage approach.

4.5.1 Image data structures

The initial image acquisition is typically in a standard RGB bitmap format. Blade surfaces usually have a light gray color, whereas surface defects as well as background noise like dust and insects appear as gray, dark gray, and black colors in field images. Therefore, grayscale images are appropriate image formats for subsequent image processing techniques. Grayscale images are represented as an m X n matrix with mn elements, each element having a pixel intensity between

0 and 255. The pixel location within an image is defined by the row and column location within the matrix (i.e. a pixel with location (a, b) means the pixel located at the intersection of row a and column b, where $1 \leq a \leq m$, $1 \leq b \leq n$).

The data structure after image segmentation is a binary format because cracks as well as other surface defects can be detected as "a sudden change of intensity in an image", which represents an edge [21]. With a threshold method, gray scale images are converted into binary images with a 0 corresponding to the normal blade surface and a 1 corresponding to noise or a crack.

4.5.2 Overview of the methods

The main steps in our method are shown in Fig. 4. First, field images in RGB format were converted into grayscale intensity images by eliminating hue and saturation information while retaining the luminance [22]. Edge detection was performed to identify points in a grayscale image at which the intensity level of pixels changes sharply (i.e., a discontinuity). A threshold value was selected by computing the signal-to-noise ratio (SNR) [23], which is defined as

$$SNR = \left(\frac{\bar{h}}{RMS}\right)^2 \tag{1}$$

where $\bar{h}$ is the average signal value (i.e., the mean pixel intensity of defects in grayscale).

RMS is the standard deviation of the intensity level of all pixels, defined as

$$RMS = \sqrt{\frac{\sum_{i=1}^{n} x_i^2 - \frac{\left(\sum_{i=1}^{n} x_i\right)^2}{n}}{n-1}} \tag{2}$$

where x_i is the pixel intensity of pixel i and n is the total number of pixels.

The SNR is easy to compute and can be applied either locally or globally. The threshold is applied to the histogram of the grayscale values, which converts the image to binary by turning every pixel with intensity level less than the threshold to 0 and 1 otherwise. The histogram is the distribution of the pixel intensity that was used in the edge detection method to convert the grayscale image to a binary image. The primary goal of the edge detection is to extract cracks defined in section 2 from a grayscale image based on its grayscale histogram.

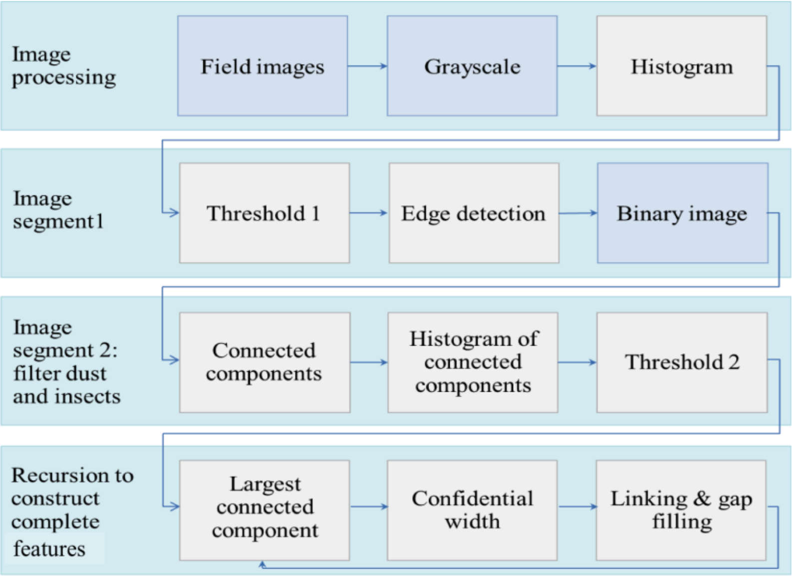

Fig. 4 Four major steps in the analysis

Background noise with intensity level higher than the interested objects (i.e. cracks in the study) can pass the edge detection filter. Thus noise included in image segmentation was eliminated in the third step when pixels with connected neighbors were grouped together to form connected components and then the cc-threshold was applied to filter out small connected components (which correspond to background noise caused by dirt and insects). Similarly, the cc-threshold was computed by the signal to noise ratio, where each connected component was treated as a pixel and the size of the connected component was considered as the intensity level of the pixel. Connected components with number of pixels larger than the cc-threshold were selected as cracks. Others were filtered out as noise that passed through the edge detection matrix. However, some unexpected background noise, for instance, the black mark in region (b) of Fig. 3, would be able to have larger number of connected pixels than the cc-threshold.

Thresholding created gaps and voids in the detected cracks as well as some “non-crack” features such as the large black marks shown in region (b) of Fig. 3. The last step in Fig. 4 estimating connections between crack segments in crack features. A recursive linkage algorithm joined crack segments starting from the largest connected components because small cracks might be branches of larger cracks.

4.5.3 Edge detection operator

We used the *Sobel* operator for edge detection because insects and dirt appeared as dots or point clouds after edge detection and these can be filtered relatively easily as compared to other methods [5]. For example, the *Canny* operator has a low error rate so that the detection catches as many edges as possible. Therefore, the background noise appeared as small segments that were difficult to distinguish from hairline cracks in this study. The *Sobel* operator calculates the average change in pixel intensity as we move from a pixel to each of its 8 neighboring pixels. If the magnitude of this change is greater than a threshold value, then the pixel is considered to be part of an edge and is assigned a value of 1. Pixels falling below this threshold are assigned a value of 0.

Given the uneven illumination of blade images, Otsu’s method did not provide a suitable threshold as explained in section 3. We found a localized threshold value based on signal-to-noise that will significantly reduce the impact of uneven illumination. Minimizing the signal-to-noise ratio is one way to minimize the classification error. By changing the threshold number, the signal-to-noise ratio will be correspondingly changed. Thus, the threshold with the smallest

SNR will be identified as the best threshold value.

4.5.4 Removing background noise

Cracks appear as connected components with a large number of connected pixels. A pixel of intensity 1 surrounded by 0s as neighbors is classified as an isolated pixel (i.e., a size of 1). A pixel with one side all 0s and the other side and both top and bottom pixels as 1s is classified as an edge pixel. By applying another threshold cc-threshold, we can eliminate the isolated pixels as well as those connected components with small number of pixels, where those connected components were defined as background noise.

To automatically determine cc-threshold, named as T_2, we used a similar approach as the edge threshold method, where SNR is the local mean of the number of pixels of connected components divided by its standard deviation. Thus, T_2 is given by

$$T_2 = \frac{\bar{x}_{pixels}}{\sqrt{\dfrac{\sum_{i=1}^{n} x_i^2 - \dfrac{(\sum_{i=1}^{n} x_i)^2}{n}}{n-1}}} \qquad (3)$$

where n is the number of connected components within the binary image after edge detection,x_i is number of pixels for connected component i, and $\bar{x}_{pixels}$ is the mean of all x_is.

4.5.5 Linkage of discontinuous fractures

Threshold-based feature segmentation leaves gaps and voids in detected features where the intensity level of defects is lower than the background noise. Also estimating connects between neighbor crack segments is more important in the study due to twice threshold applications. Therefore, a small window is necessary to fill the gaps in the detected features in order to obtain compete information. The computational steps of edge point linking are (1) select an initial edge that started from the largest connected components with high length-to-width ratio, (2) compute the directions of the edge as well as the distance to neighbor edges. (3) Apply a small window to decide whether the neighbor edges were connected. Also if there are other edges lie into the boundary box of the selected edge but the direction approximation lines were different from the selected edge, then we consider the other edges as branches of the selected edge. In this way, the neighbor edges will not be linked to the selected edge. A simple but effective edge linkage algorithm proposed by Robinson examines eight compass directions in a 3X3 pixel neighborhood as shown in Fig. 5 [24]. The arrows that connected 3 pixel spaces represent the linkage direction and the other arrows that only count 1 pixel each, represent there are neighbor pixels around.

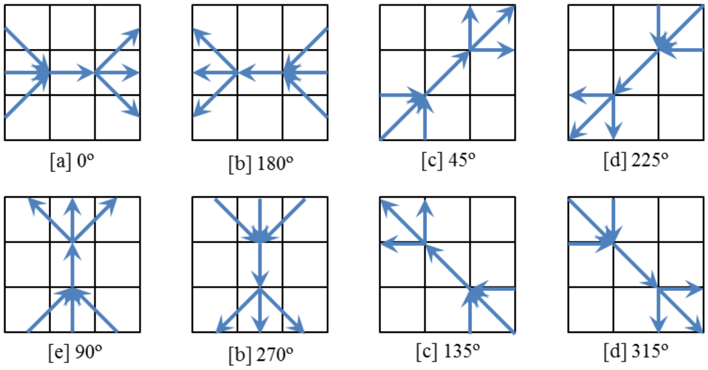

[a] 0° [b] 180° [c] 45° [d] 225°

[e] 90° [b] 270° [c] 135° [d] 315°

Fig. 5. Edge linkage directions [24].

The distance between two neighbor edges is one factor that determines whether the two edges were connected or intersected, especially defining crack branches. We used the boundary box of the selected edge, which is generated by the statistical Minimax function in which neighbor edges within a window size are considered as branches if they are lies into the boundary box with direction intersect to the deflected edge and much shorter length as the crack. The average distance between the crack segments and its nearest neighbors determined the window size. It is challenging to determine the point of attachment for a qualified branch. As shown in Fig. 6, the point in red along the selected crack can form a similar direction segment as the crack was selected to connect the branch to the crack that is marked in red in Fig. 6. One can see that the red segment has longer distance than if we linked the left end point of the branch to the point on top of it.

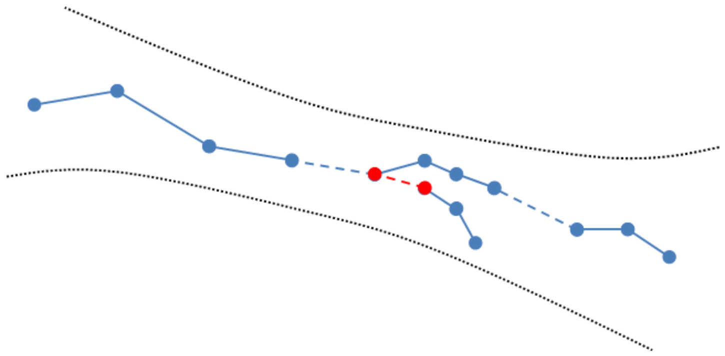

Fig. 6. Edge linkage rules. (1) Branches are only considered when smaller edges located within the band marked in black. (2) The point connected to a branch was determined by both distance and direction of the segment connected by the end point of the branch and the point on the edge.

4.6 Experiment and results

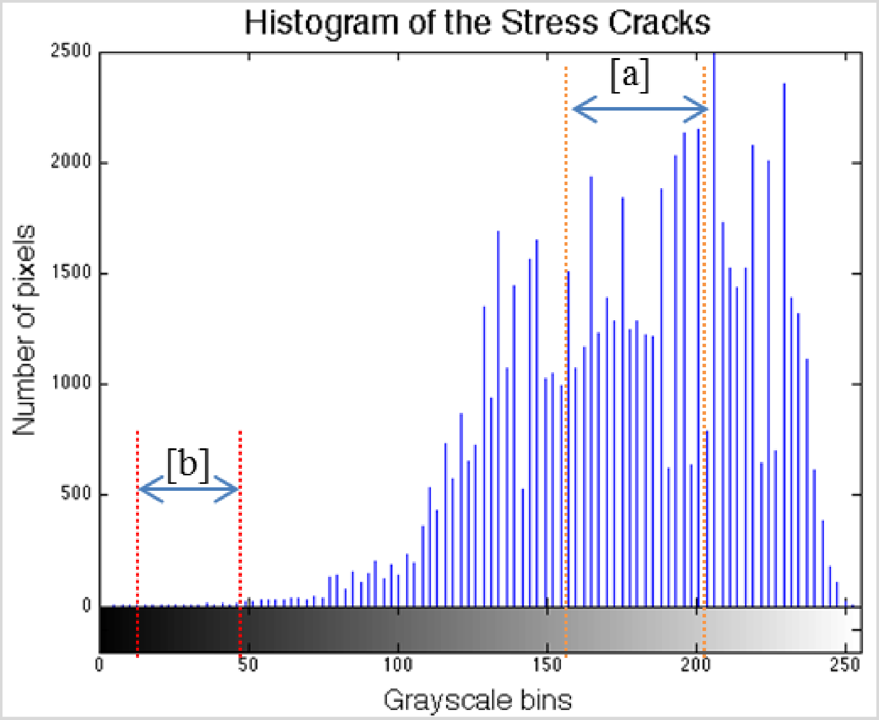

Fig. 7. Histogram of the stress cracks in Fig. 3 where region [a] has uneven illumination and region [b] has background noise.

The histogram of the stress cracks in Fig. 3 is shown in Fig. 7, where the uneven background illumination has high intensity level and the black marks in region (b) of Fig. 3 has even lower intensity level as compared to crack features as shown in Fig. 5. The regions (a) and (b) were extracted from the original image of Fig. 3. We checked its histogram separately and found out they were corresponding to the bins in Fig. 7 labeled as [a] and [b].

After edge detection with Sobel operator, we detected edges as shown in Fig. 8 (a). Some background noises were also extracted from the original image due to the low intensity level of the noises. Here we filtered the background noise using the concept of connected components. After removing all isolated pixel components from Fig. 8 (a), the total number of connected components was reduced from 537 to 329. There were no visible changes to the stress cracks themselves. However, the background noise was significantly reduced as seen in Fig. 8 (b). By removing connected components with a size < 80 pixels, the background noise in Fig. 8 was completely removed. The tradeoff is that some features of the stress cracks disappeared while the main features were retained. This noise cc-threshold for connected components, T_2, and was used to eliminate any remaining background noise after the previous operations. To compute the second threshold T_2, we treated each connected components as a “pixel” and the number of pixels within a connected component as its “intensity level of the pixel”. Then we compute the signal-to-noise ratio to generate the optimized second threshold.

To understand the background noise, we used a histogram of the size of connected components to classify features. The histogram indicates that most background noise includes connected components with a size between 0 and 20 as shown in Fig.9. It explains why Fig. 8 (c) has primarily crack features with a threshold of 20.

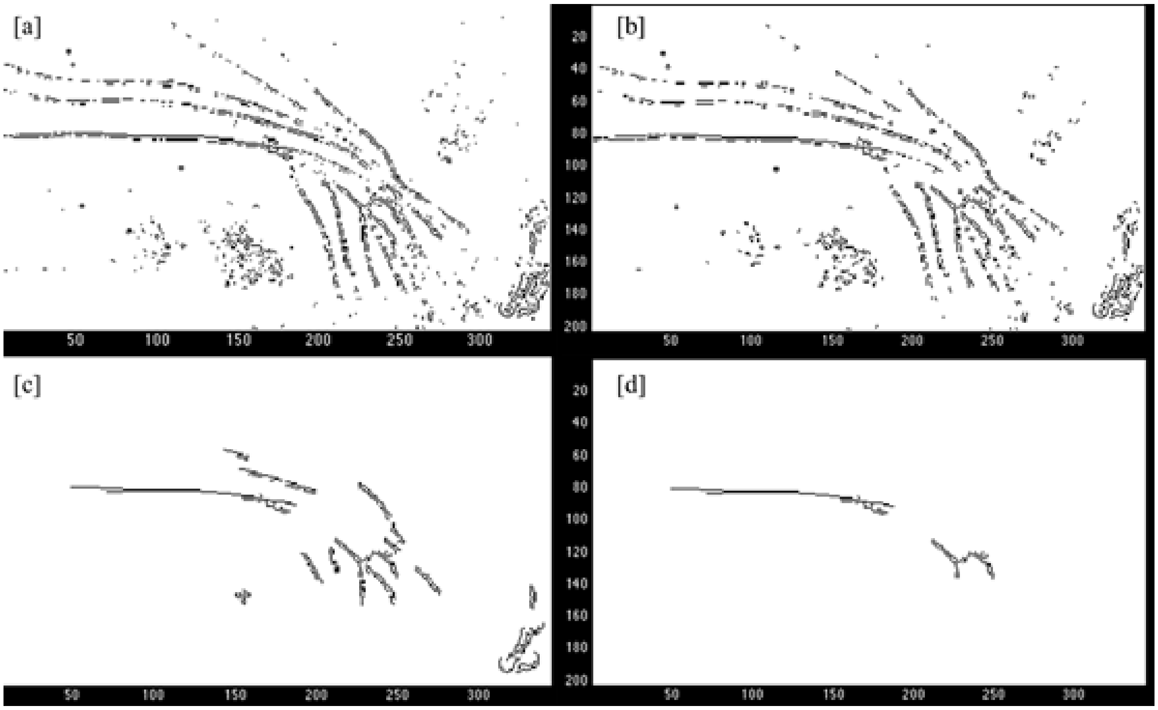

Fig. 8. Connected components concept
(a) Initial edge detection using the *Sobel* operator and the threshold from the pattern recognition method. (b) All components with a size of 1 pixel were eliminated. (c) All components with a size ≤ 20 pixels were eliminated. (d) All components with a size > 80 pixels were retained to identify the main features

The automatic thresholding value of $T_2 = 0.4231$ was obtained by the signal-to-noise ratio in section IV for Fig. 8 (a). The connected component with the largest number of pixels is on the top left of Fig. 8 (d) and it contains 185 pixels. The connected component with the smallest number of pixels is the isolated pixels in Fig. 8 (a) that looks like a single dot. We scaled the size of all connected components to a number between 0 and 1 by dividing by 185 just as we scaled intensity level of pixels by dividing by 255. Thus, the largest connected component with number of pixels 185 has intensity 1. All other connected components in Fig. 8 (a) will have intensity level less than 1. In other words, intensity level 0.4231 is corresponding to a connected component with pixel number equal to 78. Therefore, T_2 treated the connected components with the number of connected pixels less that 78 as background noise and eliminated them. Here we defined that weak defects are the connected components with fewer pixels as compared to background noise, which shows up as point clouds in the binary images after edge detection.

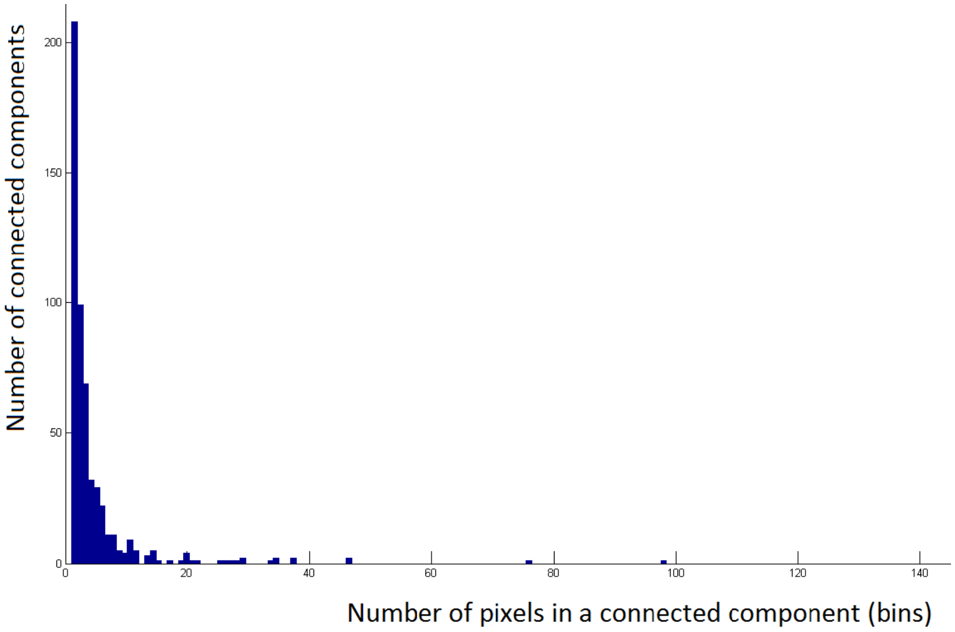

Fig. 9. Histogram of connected components.

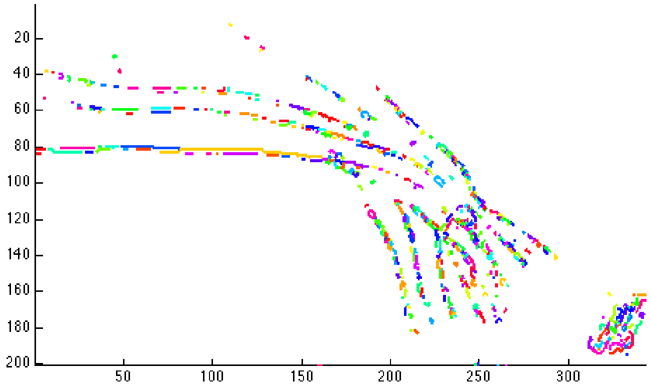

Fig. 10. Edge linkage of the stress cracks sample. The distance to determine if there is a gap existed was setup as 10 pixels.

The sample stress cracks image was processed with methods described in section IV. The results in Fig. 10 [24] show significantly less noise as compared to the binary image after edge detection (see Figure 8 (a)) and the gaps were filled with lines. Different colors represent how much linking we applied to the image when there were gaps or voids between different colors in the cracks.

4.7 Discussion and conclusion

This paper describes a new image segmentation method to reduce environmental noise as well as uneven illumination in order to increase the accuracy of wind turbine blade surface health inspection with digital images. Noise that was not removed by an edge detection method was considered as individual connected components, which was filtered based on the size of the connected components, where size corresponds to the number of connected pixels within each individual connected component. In this way, another threshold was introduced based on the histogram of the connected components and produced much clearer results by significantly reducing the appearance of insects and dirt.

The edge linkage method was applied to fill the gaps in cracks produced by the thresholding methods and to smooth the final output. The method considered both direction and distance to determine the connection points of crack branches. The confidence interval band can help limit the number of computations and the recursive function started from the edge with a maximum number of pixels to the edge with a minimum number of pixels but bigger than the cc-threshold guaranteed all edges were operated under the linkage function without cross-linking and connected to a point cloud generated by background noise. There is a significant improvement comparing the edge linking method results in Fig 10 to the previous edge detection results in Fig. 8 [a]. However, one point cloud located on the right bottom of Fig. 10 cannot be eliminated because it is the second largest connected component and the image selected in the study represented a more complex problem.

4.7.1 Pros and cons

The proposed threshold-based segmentation method has some very promising results in terms of reducing background noise such as insects and dust, especially when this noise has low intensity levels with low frequency and the cracks have high intensity as shown in Fig. 3. However, cracks in rotor blade surface images typically have low intensity pixels. When comparing Fig. 10 to Fig. 8 (a), we conclude that the proposed method can reduce background noise as well as fill gaps with a much smoother result, where the different colors marked in Fig. 10 represent the amount of linkages.

Another advantage is that the images can be stored as binary images and operations are performed in binary so that the computational time and memory space was significantly reduced as compared to other methods. This is very important for on-site wind turbine blade health inspection since reducing inspection time is equivalent to increasing turbine available period.

In addition, the edge linkage algorithm determines branches and the connected points, which were not only based on distance; but also offered much more realistic connection by examining directions. The threshold idea of removing background noise can be used to detect other defects.

While the proposed method significantly reduced background noise, it did not eliminate it completely. One can see the severe noise labeled in Fig. 3 (b) still exists in Fig 10.

4.7.2 Other considerations

There are some other points to consider before applying this method to field inspections. One is to determine the general geometries of environmental noise which can vary from one class of defects like cracks to another class like erosion. The other is to eliminate the noise located on the right bottom of Fig. 10 via feature fitting.

4.8 References

[1] M. E. Ibrahim, "Nondestructive evaluation of thick-section composites and sandwich structures: A review." *Composites Part A: Applied Science and Manufacturing*, Vol. 64, pp.36-48, Sep. 2014.

[2] N. Dalili, A. Edrisy, and R. Carriveau. "A review of surface engineering issues critical to wind turbine performance," *Renewable and Sustainable Energy Reviews*, Vol. 13(2), pp.428-438, Feb. 2009.

[3] F. Besnard and L. Bertling, "An approach for condition-based maintenance optimization applied to wind turbine blades," *IEEE Trans. Sustainable Energy,* Vol. 1, No. 2, pp.77-83, Jul. 2010.

[4] E. Sagol, M. Reggio, and A. Llinca, "Issues Concerning roughness on wind turbine blades," *Renewable and Sustainable Energy Reviews,* Vol. 23, pp.514-525, Jul. 2013.

[5] H. Zhang and J. Jackman, "Feasibility of automatic detection of surface cracks in wind turbine blades," *Wind Engineering,* Vol. 38, No. 6, pp.575-586, 2014.

[6] B. F. Sørensen, E. Jørgensen, and C. P. Debel "Improved design of large wind turbine blade of fiber composites based on studies of scale effects (Phase 1) – Summary Report," Risø National Laboratory, Denmark, Tech. Rep. Risø-R-1390(EN), Sep. 2004.

[7] K. Schroeder, W. Ecke, J. Apitz, E. Lembke, and G. Lenschow, "A fibre Bragg grating sensor system monitors operational load in a wind turbine rotor blade," *Meas. Sci. Technol.*, Vol. 17 (5), pp.1167-72, May. 2006.

[8] Z. Hameed, Y.S. Hong, Y.M. Cho, S.H. Ahn, and C.K. Song, "Condition monitoring and fault detection of wind turbines and related algorithms: A review," *Renewable and Sustainable Energy Reviews,* Vol. 13, Issue. 1, pp.1-39, Jan. 2009.

[9] P.A. Joosse, M.J. Blanch, and A.G. Dutton, "Acoustic emission monitoring of small wind turbine blades," *J. Sol. Energy Eng.* Vol. 124(4), pp.446-454, Nov. 2002.

[10] M.J. Blanch and A.G. Dutton, "Acoustic emission monitoring of field tests of an operating wind turbine," *Key Engineering Materials*, Vol.245-246, pp.475-482, Jul. 2003.

[11] G. Marsh, "Meeting the challenge of wind turbine blade repair," *Reinforced Plastics*, Vol.55(4), pp.32-36, Jul.-Aug. 2011.

[12] M. Mumtaz et al., "A new approach to aircraft surface inspection based on directional energies of texture," *Pattern Recognition, 2010 20th Int. Conf. on,* Istanbul, 2010, pp.4404-4407.

[13] M. Siegel and P. Gunatilake, "Remote enhanced visual inspection of aircraft by a mobile robot," The Robot Institute. Carnegie Mellon University. *Proc. of the Intelligent NDE Sciences for Aging and Futuristic Aircraft Workshop*, September, 1997, pp. 101–112

[14] H. R. Sheikh and A. C. Bovik (2006), "Image information and visual quality," Image Processing, IEEE Transactions on, 15(2), 430-444.

[15] N. Bonnet, J. Cutrona & M. Herbin, "A 'no-threshold' histogram-based image segmentation method," Pattern Recognition vol. 35, no. 10, pp. 2319-2322. 2002.

[16] M. Cheriet et al. "A recursive thresholding technique for image segmentation," *IEEE Trans. Image Processing,* Vol. 7, Issue. 6, pp.918-921, Jun. 1998.

[17] Y. Xia et al. "Image segmentation by clustering of spatial patterns," *Pattern Recognition Letters,* Vol. 28, Issue. 12, pp.1548-1555. Sep. 2007.

[18] N. Otsu, "A threshold selection method from gray-level histograms," *IEEE Trans. Systems, Man, and Cybernetics,* Vol. 9, No. 1, pp.62-66, Nov. 1979.

[19] B. Shah, "Implementation of image segmentation on digital images using modified Otsu

algorithm," *Int. Journal of Innovative Technology and Exploring Engineering (IJITE*E), Vol. 1, Issue 1, Jun. 2012.

[20] Uneven lighting image by Dan., Available at http://blog.dankim.com/2010/09/03/gelcoat-cracks/. Nov. 2014

[21] E. Allen and S. Triantaphillidou, "The Manual of Photography and Digital Imaging," *in Title of His Published Book*, 10th ed. Burlington, MA: Focal Press, 2009, ch. 2, pp. 27.

[22] R.C. *Gonzalez*, "Digital Image Processing Using MATLAB", *in Title of His Published Book*, 2nd ed., Upper Saddle River, N.J., Pearson Education, Inc. 2004

[23] U. Qidwai and C.H. Chen, "Digital image processing: An algorithmic approach with MATLAB," *Boca Raton*, FL: CRC Press, 2010.

[24] G.S. Robinson, "Edge detection by compass gradient masks," Note, *Computer Graphics and Image Processing*, Vol. 6, No. 5, pp. 492-501, Oct. 1977.

CHAPTER 5. CRACK RECOGNITION AND CLASSIFICATION

5.1 Abstract

In this study, we developed a crack recognition and classification algorithm in order to achieve automated structural health inspection of large composite coating materials. Unlike many existing methods that depend on comparing a single image to a library of field cracks, the proposed algorithm uses a self-learning mechanism without comparing images and can identify the type of crack automatically. Specifically, shape representation is applied to describe the characteristic of each connected component within a crack. Some key geometric properties of the connected component, like orientation and dimensions, are selected to classify the cracks based on the geometric relations between large connected components within the cracks. Further, new types of cracks may be introduced in the field, so the numerical concept is developed with unsupervised self-learning methods. Field images were analyzed to demonstrate that the proposed method can identify and classify different existing cracks, especially the three kinds of cracks defined in Chapter 3. In addition, the study addresses the issue of learning to recognize new types of cracks.

5.2 Introduction

This chapter addresses the last part of the second research question: (2) can an image-processing model be formulated that reduces the uncertainty of image processing results while identifying blade surface flaws? This chapter explains how to use image processing to better recognize and classify cracks. This method enables wind farm owners and operators to better prioritize repair work. Finally, a discussion of the third research question is presented: (3) what are the important elements of an uncertainty model that can improve the detection results for real-time on-site inspection and how are they related?

Current practice requires engineers to visually identify the severity of a crack, classify the type of crack, and determine other information like the location of the defect along the surface of a WTB so that a repair decision can be made. This process is heavily dependent on the engineer’s experience level as well as proper communication between the on-site technician and the engineer. Thus, the uncertainties involved in the crack recognition can result in incorrect repair decisions and further damage to the turbine. In addition, engineers and on-site technicians are responsible for multiple wind farms, leading to problems like transferring and managing large sets of images, as well as missing inspection information. These problems introduce uncertainties between engineers and on-site technicians. Current practice makes it difficult to document cracks in a well-structured form that can be used for future reference, especially for those blades with more than one type of failure history and different repair procedures. Therefore, it would be beneficial to develop a crack recognition and classification algorithm that supports the decision making process and reduces inspection uncertainty.

Computer or machine-aided vision underwent rapid growth in the late 1960s with the goal of recognizing objects and the relationship between objects by comparing image processing with natural vision systems. Early studies focused on individual, restricted objects by extracting features (e.g., edges, lines, and regions) from images. These features were then compared with previously stored images (a library) and the best match was selected as the “visual recognition” of the object [1]. Although the pre-existing library approach was limited to known objects, the concept of extracting features continues to be widely accepted in the visual recognition research community.

The second generation of vision studies focused on 3D objects by describing 3D shape information such as depth, orientation, and reflectance [2]. The 3D technology was applied in the

1970s and most of the vision techniques were adopted for 3D machining and robotics. Lately, researchers have attempted to apply human vision concepts to machine vision without prior knowledge of the objects. Since human vision performs well at structuring low-level representations, studies have focused on specific areas such as continuity, regions, and curves of objects [3]. In our study, we adopted feature extraction methods and applied human vision concepts to avoid the limitations of prior stored images.

Segmentation is one of the most important steps in object recognition and different approaches have been developed for object recognition purposes. One approach is based on shape masks, which carry information about the outline of the objects [4]. The challenge of shape masks is to apply the most appropriate shape mask for a specific object. Shape matching or shape representation applies segmentation to an image and detects the geometric relationships of the boundary edges of the objects [5]. Based on the geometry of the boundary edges of the objects, the objects can be identified and classified into different categories. The method can identify known objects efficiently but can also describe the geometric relationships of unknown objects. However, the segmentation-based methods generally have difficulties when the intensity level of all the pixels of the objects is inconsistent.

5.3 Methodology

5.3.1 Overview

The shape representation concept was used as a basis for the crack recognition and classification methods described in this study. For a given image, we first determine how many "potential cracks" exist based on the edge detection results where the edges are segmented from the original image and the edges are a set of connected components. A connected component is a set of connected pixels as explained in Chapter 3. The next step is to select a subset containing the largest connected components of a “potential crack” and address the geometric properties of each connected component as well as the geometric relationships between the connected components. The geometric properties of each connected component are important to determine if it is a crack or other defect. For example, a connected component having a large ratio between the major axis length and minor axis length of the enclosing ellipse can be a crack but not necessarily. Other geometric properties have to be addressed to support the determination that it is a crack. The geometric relationships between the selected connected components can be used to classify the crack type. For example, connected components with a parallel relationship are likely to be stress cracks as described in Chapter 3. We introduce the term “potential crack” to describe a defect appearing in a field image that could be a crack or other object such as noise.

5.3.2 Threshold of connected components

The histogram of connected components shown in Chapter 4 Fig. 9 had a right skewed distribution, where 90% of the connected components had fewer than 10 pixels. To classify a given crack, the behaviors of the largest connected components play an important role in defining the crack structure while the small connected components can be noise or isolated pixels that do not significantly affect the geometric properties of the crack. Therefore, only the set of largest connected components were studied. Based on the histogram of the 27 field images studied in Chapter 3, we observed that the top 10 percentile of the connected components was sufficient to recognize and classify a crack.

The rest of the connected components were either background noise or small parts of a crack that was generated by image segmentation. Neither of them was large enough to represent the geometric structure of a crack. The skewness of the distribution of component size of the connected components was used to eliminate the background noise and other small objects. The results contained much more noise objects as compared to the top 10 percentile.

Using the top 10 percentile of objects as a threshold can eliminate the background noise but not all connected components within the top 10 percentile are useful for classifying cracks. The method proposed here is to sort the objects by size in descending order and analyze them in sorted order. One issue that needs to be addressed is the stopping condition. Do we need to examine all the connected components within the top 10 percentile? The study of the 27 field images showed that the mean value of the number of pixels in a component for the top 10 percentile of all the connected components is a feasible threshold to reduce the number of connected components necessary for recognizing and classifying a crack.

5.3.3 Geometric properties of a connected component

Each connected component has a set of geometric properties that can be computed relatively easily. These properties describe different characteristics of the shape of a connected component and can be used to classify the type of the crack. As shown in Fig. 1, the major axis length is the length of the longest axis of a connected component and the minor axis length is the maximum length that is perpendicular to the major axis. The major axis length is determined by "the length of the major axis of the ellipse that has the same normalized second central moments as the region". The minor axis length is determined by the minor axis of the same ellipse. The centroid represents the center of the mass, which is the average of the x and y values for the pixel locations. The bounding box encloses the connected component as we described in Chapter 3. The bounding box is a rectangle that connects the points with a minimum value of x, minimum value of y, maximum valve of x, and maximum value of y. The orientation returns the angle between the major axis and the x-axis of the image that is useful to represent the orientation and growing direction of the crack. Another important property is the area that shows the number of connected pixels. The *regionprops* function in Matlab returns the geometric properties for any given image. However, the centroid represents the center of the mass and cannot be used to accurately determine the start and end points of the major axis since it is not necessary on the major and minor axes. An alternate solution is to apply the midpoint of each axis to compute the start and end points of each axis since the midpoint with respect to the x and y axes is always on the axes. Once the start and end points are computed, we can draw the axis easily for a component.

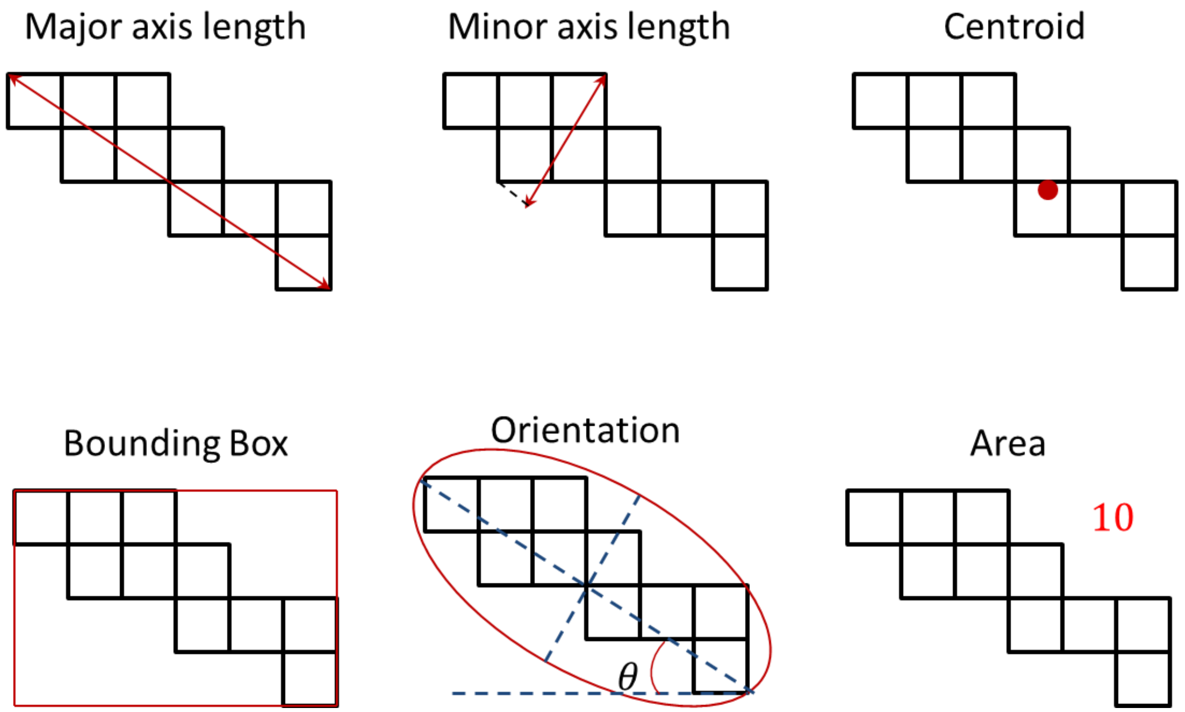

Figure 1. Geometric properties of connected components.

As shown in Fig. 1, the start and end points of the major and minor axes can be computed by

$$x_{st/end} = x_{midpoint} \mp \frac{1}{2} * MajorAxisLength * \cos\theta \ldots (1)$$

$$y_{st/end} = y_{midpoint} \pm \frac{1}{2} * MajorAxisLength * \sin\theta \ldots (2)$$

where ($x_{st/end}$, $y_{st/end}$) represents the start and end points of the major axis, ($x_{midpoint}$, $y_{midpoint}$) is the midpoint of the major axis, and θ is the angle between the major axis and the x axis of the image.

5.3.4 Geometric properties between connected components

A crack is constructed from multiple connected components due to (1) the discontinuity of the crack itself in the field images and (2) the voids/gaps generated by image processing methods. The geometric properties between the connected components of a given crack were used to determine the type of the crack. One of the examples is a hairline crack where each connected component shares a similar slope for the major axis and the coordinate of the end point of one connected component is near the start point of the neighbor connected component. Also, the ratio between the major axis length and the minor axis length is large. The crack classification method based on the geometric properties is shown in Table 1.

Table 1. Crack classification based on geometric properties

Type	Asymmetry	Orientation	Proximity
Hairline crack	R > 5*	Slope ∈ (mean ± one s.d.)	End point of one connected component and the start point of the next connected component has x value within 1 minor axis length and y value in ascending order
Stress crack	R > 5	Slope ∈ (mean ± one s.d.)	Start and end points with with x (or y) value within 1 s.d. and y (or x) value larger than 1 s.d.
Crazing crack	R < 5	Enclosed by polygon which has the smallest area and > 4 edges	A smaller polygon with edges parallel to the previous polygon has the number of intersection points with the cracks equal to the number of its edges.

*R is the ratio of the major axis length to minor axis length and describes the asymmetry of the object (R = 1 is a symmetric object). The number 5 was selected based on the histogram of the major axis to minor axis ratio.

There are more crack types that can be represented with the geometric properties between connected components. For an unknown type of a crack, a new class can be defined based on its geometric properties that will classify cracks with a similar shape. Thus, the method depends on a classification method and is not dependent on a pre-set library of known images.

5.4 Results

The histogram of the hairline crack shown in Fig. 2, in which the noise components were filtered out, has a mean size of 28 pixels for the remaining connected components. There are 5 connected components larger than the mean value, which is placed in the top 10 percentile addressed in Chapter 5.3. Therefore, we studied the characteristics of the 5 largest connected components and the relationships between them to determine the type of the crack.

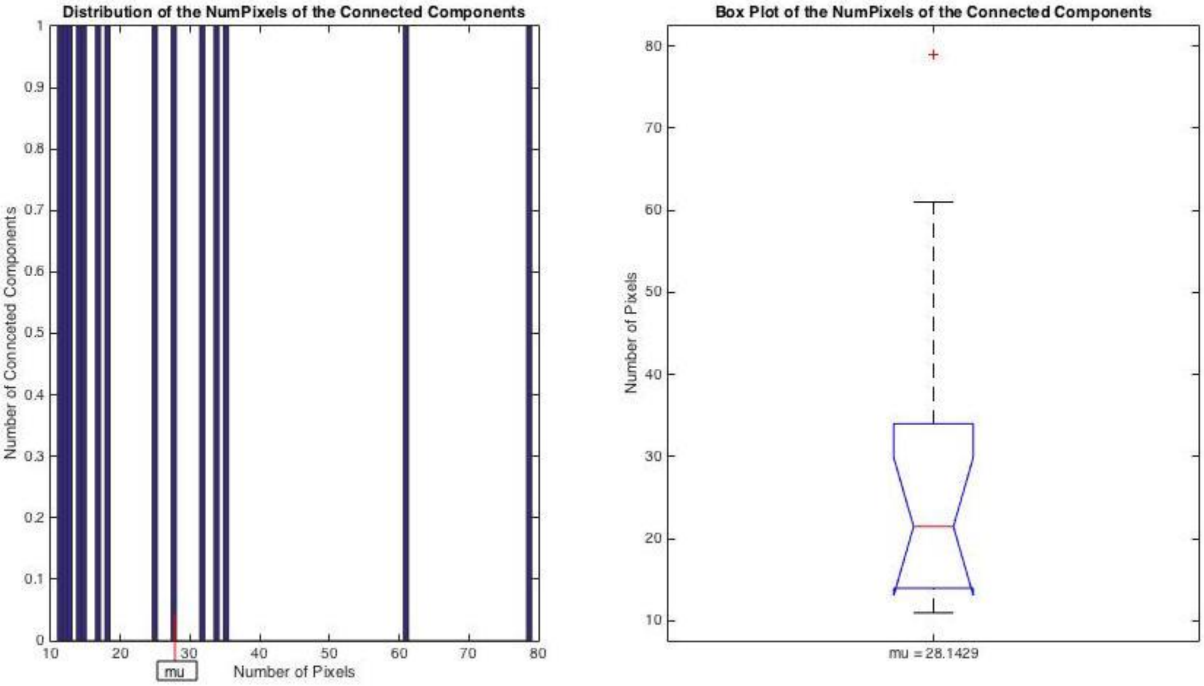

Figure 2. Histogram and boxplot of hairline crack.

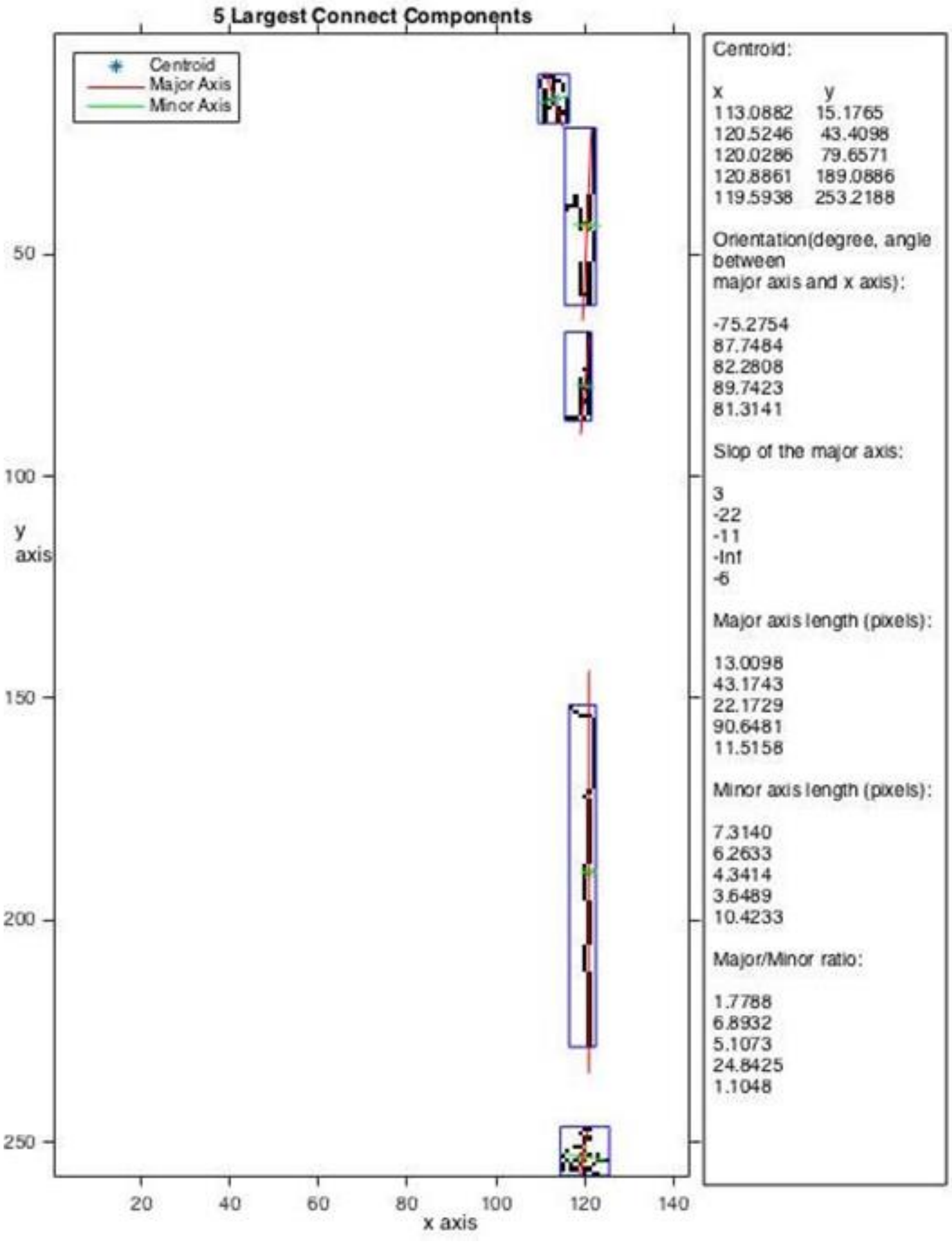

```
Centroid:

x            y
113.0882   15.1765
120.5246    43.4098
120.0286    79.6571
120.8861   189.0886
119.5938   253.2188

Orientation(degree, angle
between
major axis and x axis):

-75.2754
87.7484
82.2808
89.7423
81.3141

Slop of the major axis:

3
-22
-11
-Inf
-6

Major axis length (pixels):

13.0098
43.1743
22.1729
90.6481
11.5158

Minor axis length (pixels):

7.3140
6.2633
4.3414
3.6489
10.4233

Major/Minor ratio:

1.7788
6.8932
5.1073
24.8425
1.1048
```

Figure 3. Geometric properties of the 5 largest connected component of the hairline crack.

The results shown in Fig. 3 shows that the centroid points of the largest 5 connected components are located along one vertical line (x = 120), indicating that the crack is growing vertically. The orientation of the connected components also supported the vertical orientation of the defect since the slope of each object is within the range of mean ± one standard deviation. Considering the connected components with $R > 5$, the image's largest 3 connected components met the criteria with relatively small minor axis length, ≤ 7 pixels, which indicates that the defect is probably a vertically oriented hairline crack. For example, the largest connected component of the image had an $R > 24$ and the minor axis length is only 3.6 pixels. The major axes of the connected components shown in Fig. 3 as red lines are further support for the hairline crack classification.

The stress crack introduced in Chapter 3 had a mean connected component size of 22 pixels after eliminating the background noise by taking the top 10 percentile of connected components. There were 20 connected components larger than the mean (see Fig. 4). Thus, we analyzed the geometric properties of the largest 20 connected components (see Table 2) and classified the crack based on the geometric relationships between the components. There were 15 connected components orientated between 0 and 50 degrees from the upper left to the lower right area of the image and some of them have exactly same orientation/slope with centroid data indicating they are parallel to each other. However, there were also 5 connected components with the opposite orientation that were marked in red in Table 2. In addition, the 5 oppositely oriented connected components have major axis to minor axis length ratio smaller than 5 that indicated they are probably large background noise. Checking the noise at the bottom right corner of the stress crack image as shown in Chapter 4 Fig. 1 [b], we confirmed that the 5 connected components are severe background noise. Therefore, the image contains a stress crack with numbers of parallel small cracks that extend horizontally to -50° along the coating surface.

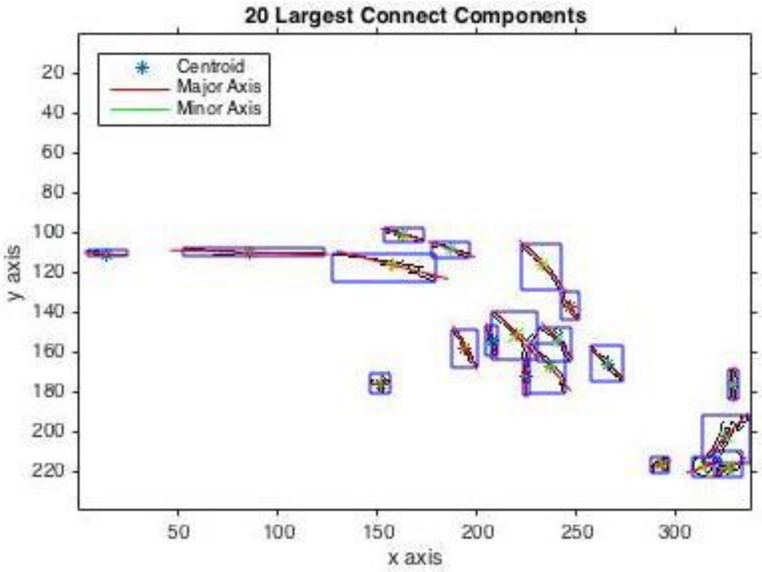

Figure 4. Geometric properties of the 20 largest connected component of the stress crack.

Table 2. Key geometric properties of the 20 largest connected components of the stress crack

Slop	Orientation (º)	Major axis length (pixels)	Minor axis length(pixels)	Centroid
0.0909	-5.3216	22.9058	2.7994	(13.7826 110.5217)
0.0250	-1.2480	79.1356	3.2276	(85.9878 109.6829)
0.2500	-13.4701	58.3817	6.1260	(157.6709 116.0506)
0	0.6871	9.8275	9.1085	(151.8929 175.5714)
0.2727	-14.9272	23.0452	3.6051	(162.9310 100.8621)
0.3333	-18.1979	24.6518	3.9560	(187.3214 108.1786)
1.8333	-59.7127	24.7327	3.7532	(194.2353 157.6176)
3.0000	-73.2311	18.3336	3.8938	(207.6538 154.2308)
1.0909	-47.4518	32.8081	11.0163	(219.8113 151.0943)
1.0833	-47.4599	34.8688	4.5681	(233.1739 116.1957)
Inf	-89.4420	18.0974	3.3988	(224.8846 172.0000)
1.1818	-50.6786	34.5344	5.7183	(236.8696 166.9565)
1.1250	-50.0423	24.0329	7.4136	(240.7500 154.0455)
1.4000	-56.2323	17.1583	4.0970	(246.5833 137.0417)
1.0000	-47.2930	25.4288	4.2069	(265.7429 165.7429)
-0.4000	18.5948	11.2735	7.8116	(292.8000 216.3600)
-0.3333	16.5333	18.1514	11.7043	(314.5357 217.3929)
-1.0909	47.7476	32.2355	9.0714	(325.4500 202.2250)
-0.5556	29.6814	19.9146	7.8519	(326.8286 217.8000)
-Inf	89.7767	17.3206	5.1273	(329.2000 176.0000)

Yellow: parallel cracks; red: noises with major-minor axis ratio < 5 and opposite orientations.

After eliminating the background noise, the distribution of the connected components size of the crazing crack had a mean value 46 and there were 14 connected components containing more than 46 pixels. For the largest connected component, R = 3.13. The component was enclosed in the convex polygon with the smallest area, which resulted in the 6-sided polygon shown in Fig. 5. Similarly, we applied the polygon concept to four other connected components with R < 5 and each polygon had more than 15 edges in order to enclose the components with minimized area as shown in Fig. 5. A smaller polygon (the length of each edge was half of the original polygon) parallel to the previous one had 6 intersection points with the crazing crack, which is equal to the number of edges of the previous polygon as shown in Fig. 5. Therefore, the crazing crack was identified and it was formed by a set of intersecting cracks. On the other side, we applied the same method to the other 4 non-crack objects. The number of intersection points between the smaller polygon and the non-crack object was different from number of the original polygon edges. Thus, only the largest connected component was classified as crazing and the other four connected components were classified as severe background noise.

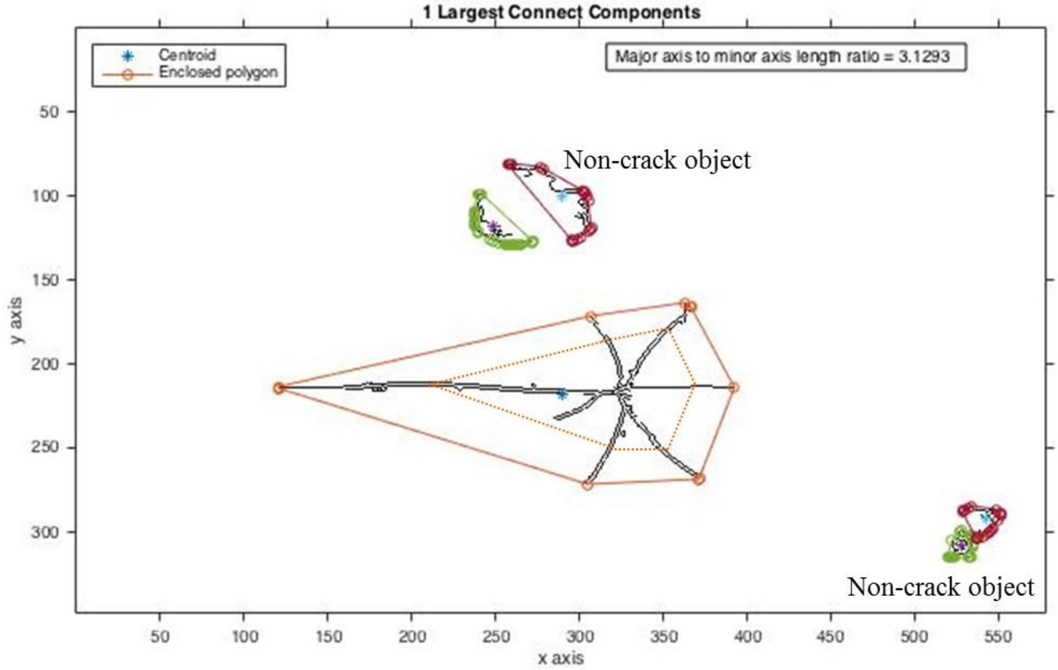

Figure 5. Geometric properties of the 20 largest connected component of the stress crack.

The histogram of R for the 14 largest connected components showed that only five connected components had R < 5 in Fig. 6. and they are the four severe background noise types and the largest connected component as shown in Fig. 5. In addition, the largest connected component was enclosed by a 6-edge polygon and a reduced size polygon parallel to the original one intersected the largest connected components with 6 points. Thus, we further confirmed the image contains a crazing crack as defined in Table 1. The left 9 connected components all had length ratio larger than 5. Considering their orientations, we concluded that the 9 connected components were individual cracks that oriented toward the largest connected component. The detailed steps were not listed here since they were similar to what we did for the stress cracks.

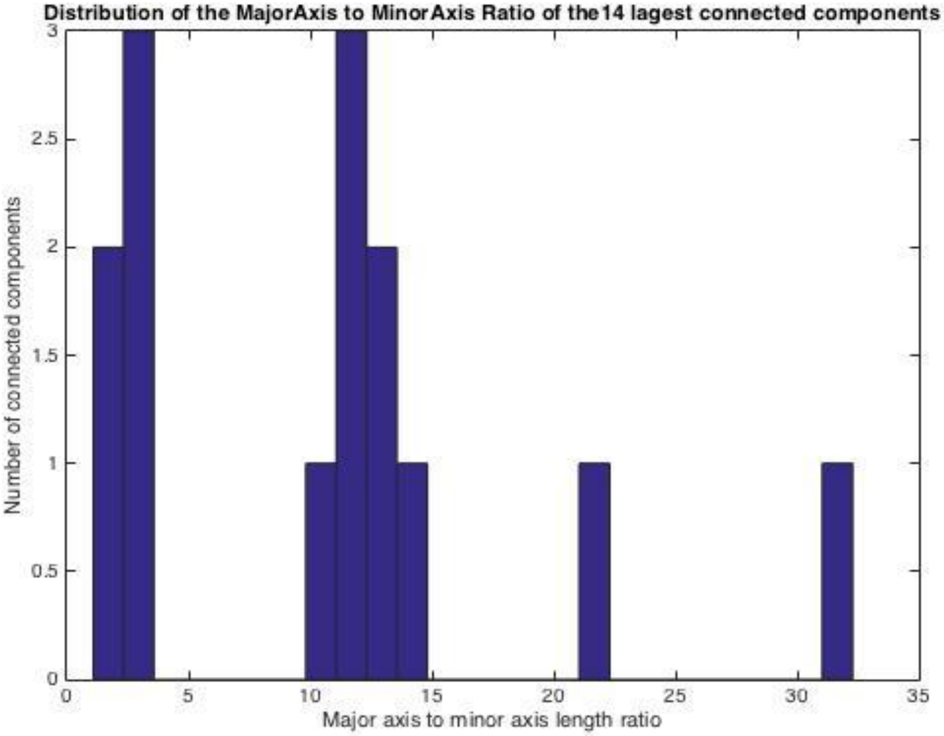

Figure 6. Histogram of the 14 largest connected components of the crazing crack.

5.5 Conclusion

This paper describes a new shape based method to recognize and classify different cracks as well as eliminate large background noise that remains after edge detection methods. The orientation, centroid, the major axis to minor axis length ratio and other geometric properties are used to characterize the type of crack. For undefined cracks, we need to further characterize their geometric properties and at least the majority of connected components should have major to minor axis length ratio larger than 5 to meet the basic requirement of a crack. Then the method can classify them into a new category if there are unique relationships between the largest connected components. In addition, the method provides some insight on the growing direction of a stress crack so that an engineer can make an informed decision about a repair plan or further inspection.

5.6 References

[1] R. T. Chin and C. R. Dyer, “Model based recognition in robot vision,” ACM Computing Surveys, Vol. 18, no. 1, pp. 67-108, 1986

[2] J.D. McCafferty, “Introduction,” in *Human and Machine vision,* 1st ed. Chichester, West Sussex, England. Ellis Horwood Limited, 1990, ch. 1, sec. 1.2.2, pp 4 -5.

[3] J.D. McCafferty, “Introduction,” in *Human and Machine vision,* 1st ed. Chichester, West Sussex, England. Ellis Horwood Limited, 1990, ch. 1, sec. 1.3, pp 6 -8.

[4] M. Marszalek and C. Schmid, “Accurate object recognition with shape masks.” *International Journal of Computer Vision*, Vol. 97, Iss. 2, pp 191-209, 2012

[5] A. Toshev, B. Taskar, and K. Daniilidis, “Shap-based object detection via boundary structure segmentation.” *International Journal of Computer Vision*, Vol. 99, Iss. 2, pp 123-146, 2012

CHAPTER 6. REDUCING UNCERTAINTY OF IMAGE SEGMENTATION IN FIELD INSPECTION OF WIND TURBINE BLADES

6.1 Introduction

This part of the study addresses the third research questions: (3) what are the important elements of an uncertainty model that can improve the detection results in real-time on-site inspections and how are they related?

In Chapter 3, we formulated and tested an inspection method that can eliminate most of the background noise as well as the effects of uneven lighting on sample stress cracks. In this study, further improvements in the method were investigated to cover more complex field conditions. In addition, the paper addresses how our method can improve the accuracy of a UAV-based inspection system.

WTBs are illuminated by varying amounts of sunlight during the day. Uneven illumination of the blade surface is caused by different positions of the sun and weather conditions, leading to uncertainty in image segmentation results that are used to identify cracks and determine blade orientation and location. Additional contributions to accurate segmentation include background noise, which can have a much higher intensity level of pixels and a similar contour as gel coat erosion, as well as dust and insects.

The image segmentation process introduces information loss by transforming low intensity pixels into background information and extracting high intensity pixels as part of an object of interest. Unlike other common applications such as satellite images, WTB images have homogenous color, fewer reference lines, and the objects of interest (flaws) can be extremely small compared to the full image. This can lead to Type I and II errors, which will increase unnecessary maintenance costs or conceal the need for early maintenance [1,2]. A Type I error in this context is a false alarm and a Type II error is not detecting a defect. Therefore, it is essential that the uncertainties in image segmentation (e.g., uneven field lighting and background noise) be addressed, especially for common field condition scenarios.

6.2 Methodology

6.2.1 Overview

In this section, a new method is proposed for reducing the uncertainty in image segmentation under uneven field lighting and environmental noise conditions. The first stage of the method focuses on uneven lighting based on Otsu's bi-level thresholding method and Huang's adaptive wind size algorithm. The second stage of the method focuses on solving the initial window size problem of Huang's method. Both stages use Zhang and Jackman's method described in Chapter 3, in which environmental noise is filtered out using a threshold for the histogram of connected components. In section 6.2.2, the detectability limit of the proposed method (i.e., the minimum detectable size of defects) is described. Following this, Otsu's method and Huang's method are briefly explained in sections 6.2.3 and 6.2.4, respectively. To examine how Otsu's method and Huang's method behave with field images of wind turbine blades, one field image was selected and the level of uneven lighting was varied in section 6.2.5. The results are presented in section 6.3.

6.2.2 Detectability

Hairline crack

Hairline cracks by definition have very small widths with low intensity level pixels in the digital image. Theoretically, a crack of one or more pixels in digital images can be detected by image segmentation if there is an intensity level difference between the crack and the background. Barely visible hairline cracks were defined by Ropeworks as having a width of 3 pixels (as shown in Figure 3 (a) in Chapter 3). The intensity level of pixels along the hairline crack has an average value of 196, where the average intensity level of the background is 201. An intensity level of 255 represents white and 0 represents black. Let the intensity level of a pixel be denoted as a function $\mathrm{f(x,y)}$, such that $0 \leq \mathrm{f(x,y)} \leq 255$ and $\mathrm{(x,y)}$ is the location of the pixel.

For any crack with size mn (i.e. the enclosing rectangular envelope has m rows and n columns), without loss of generality, assume there is a one-to-one relationship between the area of the blade surface and the number of pixels in the corresponding image. Then

- ○ $|(x_n, y_i) - (x_1, y_i)| \geq 3$, for some $1 \leq i \leq m$ and $m \gg n$

  (i.e., $width(hairline\ crack) \geq 3pixels$)
- ○ $\overline{f_b(x,y)} - \overline{f_o(x,y)} \geq 5$, where $\overline{f_b(x,y)}$ is the average intensity level of the background and $\overline{f_o(x,y)}$ is the average intensity level of the object (hairline crack). The threshold of 5 was selected based on the published hairline crack as shown in Figure 1 (a) in Chapter 3. The hairline crack has an average intensity of the object is 196 and the average intensity of its background is 201, resulting an intensity difference of 5 between its background and the crack itself.

These thresholds define the crack detection limits under typical inspection conditions to be (1) at least three pixels in width and (2) at least five intensity levels difference between the pixels of the crack and its background. Here we define the width of a hairline crack as the span of the cross section perpendicular to the line direction.

Previously, we compared the inspection results from the image segmentation method and platform-based visual inspection and showed that there was a positive correlation between the size of the defects in millimeters to the number of pixels in digital images. In these images, 1 pixel was approximately 0.55mm [21]. Thus, the minimum width of the hairline thickness cracks is on the order of $1.65\mathrm{mm}$, where 3 pixels times 0.55mm/pixel is 1.65mm. However, the detectability is highly dependent on how the image is acquired (e.g., focal length, distance from the blade, or sensor resolution).

6.2.3 Otsu's method

Bi-level thresholding-based image segmentation transforms a gray scale image $\mathrm{f(x,y)}$ into a binary image $\mathrm{g(x,y)}$ using a threshold T such that

$$g(x,y) = \begin{cases} 0 & if\ f(x,y) \leq T \\ 1 & if\ f(x,y) > T \end{cases}.$$

The gray scale image has L gray levels in the interval $(0, L-1)$. The threshold value is $T,$ such that $0 < T \leq L-1$. Using T, the image, $f(x,y)$, is divided into two groups, A (one or more objects) and B (the background). To find T, the variance associated with the two groups is computed, where $\sigma_B^2(t)$ is the variance between the objects and the background and the total variance of the image $f(x,y)$ is denoted as $\sigma_I^2(t)$. The value T^* corresponding to the largest value of $\sigma_B^2(t)/\sigma_I^2(t)$ is the best threshold is given by

$$\{T^* = t \colon \eta(t) = \max\left(\frac{\sigma_B^2(t_i)}{\left(\sigma_I^2(t_i)\right)}\right), 0 < i \leq L-1\}.$$

Using T^*, the image pixels are divided the into the two groups: A having $g(x,y) = 1$ and B with $g(x,y) = 0$. We define $\left(\omega_A(t), M_A(t)\right)$ and, $\left(\omega_B(t), M_B(t)\right)$to be the number of pixels and the average gray intensity level in groups A and B, respectively. For example, $\omega_A(t)$ represents the number of pixels in group A and $M_A(t)$ represents the average gray intensity level of all the pixels in group A. Let n_i be the number of pixels with gray intensity level i. Then

$$\omega_A(t) = \sum_{i=0}^{t} n_i,$$

$$M_A(t) = \frac{\sum_{i=0}^{t} i \cdot n_i}{\omega_A(t)},$$

$$\omega_B(t) = \sum_{i=t+1}^{L-1} n_i, \text{ and}$$

$$M_B(t) = \frac{\sum_{i=t+1}^{L-1} i \cdot n_i}{\omega_B(t)}.$$

Next, the average gray intensity level of all pixels in image $f(x, y)$ is given by

$$\mu(t) = \overline{M(t)} = \frac{\omega_A(t)M_A(t) + \omega_B(t)M_B(t)}{\omega_A(t) + \omega_B(t)}$$

and the population variance is given by

$$\sigma_I^2(t) = \frac{\sum_{i=0}^{L-1} \left(i - \mu(t)\right)^2 \cdot n_i}{N}.$$

where $N = \sum_{i=0}^{L-1} n_i$ is the total number of pixels in image $f(x, y)$. Then the variance between two groups is computed as

$$\sigma_B^2(t) = \omega_A(t)(M_A(t) - \overline{M(t)})^2 + \omega_B(t)(M_B(t) - \overline{M(t)})^2.$$

Suppose an image has L gray intensity levels, then we need to compute the threshold $\mathrm{T} = \sigma_\mathrm{B}^2(\mathrm{t})/\sigma_\mathrm{I}^2(\mathrm{t})$ L times and the best threshold is $\mathrm{T}^* = \max(\mathrm{T_i})\,, 0 \le \mathrm{i} \le \mathrm{L} - 1$, where $\mathrm{T_i}$ is the threshold for each gray level of the interval (0, L – 1). In other words, the threshold T* maximizes the variance between objects and background while minimizing the population variance.

6.2.4 Adaptive window size

Otsu's method works well for images with a significant difference in pixel intensity level between an object and its background. As a result, Otsu's method has become one of the most popular methods in the past 20 years. However, Otsu's method performs poorly under uneven lighting conditions. One way to improve Otsu's method in these conditions is to partition the image into multiple sub-images with an adaptive window size (in which the lighting is more uniform) and apply Otsu's method to each sub-image separately. Huang proposed an adaptive window size algorithm based on the Lorentz information measure (LIM) with the following steps.

Step 1. Divide the image $f(x, y)$ into mn windows of equal size, where each window size is $a \: X \: b$ as shown in Figure 1, m is the number of sections of rows and n is the number of sections of columns. Suppose the size of the image $f(x, y)$ is $M \: X \: N$, we have $M = am$ and $N = bn$. For each window k, the LIM number is defined as its grayscale value (the LIM number is explained in the next paragraph).

Step 2. Treat each window as a 'pixel' and the intensity level of each 'pixel' is the LIM number of the window (how to compute the LIM number is explained in section 6.2.4.1). Then we define a new image with mn 'pixels', denoted by $f'(x, y) = \{window\ 1, window\ 2, \cdots, window\ mn\}$. Applying Otsu's method, we obtain a threshold number T' for the new image $f'(x, y)$.

Step 3. Apply T' to threshold those pixels in the windows of $f(x, y)$ such that LIM > T'.

Step 4. For window k, if LIM $\leq T'$, enlarge window k into window K, where window K combines windows k, k+1, k+m, and k+m+1 as shown in Figure 1. Again, form a new image $f''(x, y) = \{window\ 1, window\ 2, \cdots, window\ mn, window\ K\}$ and apply Otsu's method to $f''(x, y)$ to obtain a new threshold number T''.

Step 5. For each window, check if LIM $\geq T''$. If not, repeat step 4 and in the worst case, the window K becomes the entire image.

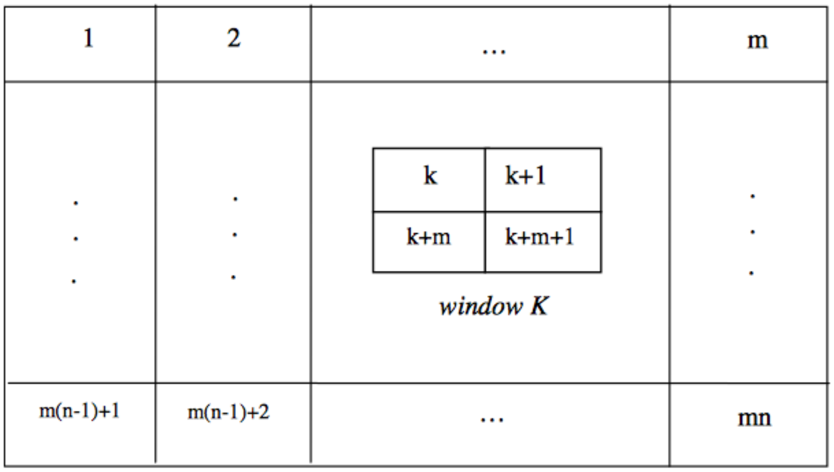

Figure 1. Adaptive window size.

6.2.4.1 Lorentz information measure

The LIM is the area under the Lorentz information curve. To create the Lorentz information curve, we need to compute the picture information measure PIM, which is given by

$$PIM(f) = \sum_{i=0}^{L-1} h(i) - max_i h(i)$$

where L is the maximum gray level of the image $f(x, y)$ and $h(i)$ represents the gray level histogram of $f(x, y)$ (i.e., $h(i)$is the number of pixels with a gray level of i).

Given that the total number of pixels in an image $f(x, y)$ is $N(f)$ (f representing the image $f(x, y)$), then the normalized picture information measure (NPIM) is defined by $\mathrm{NPIM(f)} = \mathrm{PIM(f)/N(f)}$. The probability of pixels having a gray level of i is $p_i = h(i)/\mathrm{N}(f)$, $\mathrm{NPIM(f)} = 1 - \max(\mathrm{p_i}),\ 0 \leq \mathrm{i} \leq \mathrm{L} - 1$. The generalized NPIM for level j is $\mathrm{NPIM_j(f)} = 1 - \sum_{\mathrm{i} \in \mathrm{p(j)}} \mathrm{p_i}$ for $0 \leq \mathrm{j} \leq \mathrm{L}$. In other words, $0 = \mathrm{NPIM_L(f)} \leq \mathrm{NPIM_{L-1}(f)} \leq \cdots \leq \mathrm{NPIM_0(f)} = 1$. The normalized picture information measure at each gray level as $\mathrm{S_j} = \mathrm{NPIM_{L-j}(f)}$. Therefore, $\mathrm{S_0} = 0$, $\mathrm{S_L} = 1$, and $\mathrm{S_j} = \sum_{\mathrm{i}=0}^{\mathrm{j}-1} \mathrm{p_i}$. An example of the Lorentz information curve is shown in Figure 2.

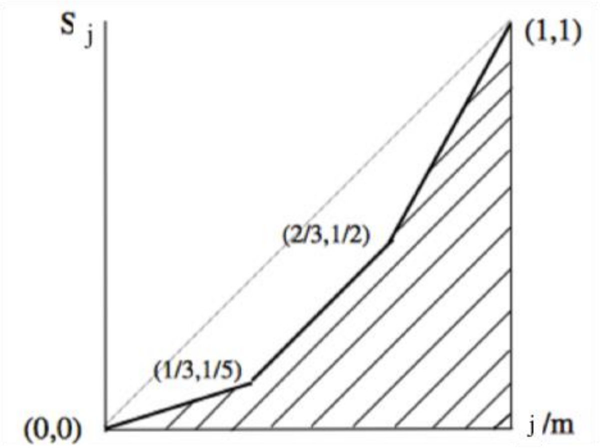

Figure 2. An example of Lorentz information curve of L = 3.

6.2.5 Field images of artificial uneven lighting

Uneven field lighting causes problems when determining the Otsu threshold number for the image, resulting in the incorrect classification of pixels. In order to investigate the effects of uneven field lighting, we studied existing field inspection data and generated artificial uneven lighting by applying 3-dimentional lights to 2-dimentional field images in Photoshop CC 2014. For example, the field image shown in Figure 3 has a significant number of hairline cracks with a consistent background illumination. Hairlines cracks are located across the entire image.

To create the type of light effects that might occur in the field, two kinds of artificial lights were studied.

A spotlight represents a beam of sunlight coming out from clouds

> This type of lighting usually appears on the leading edge of the blade in field images. The spotlight can appear near or on the cracks, depending on the position of the location of the image-capturing device with respect to the light.

An infinity light can be used to control the amount of direct sunlight.

This type of lighting most frequently occurs on field images of the blade with large smooth blade surfaces.

Figure 3. Parallel gel coat cracks.

The same spotlight was applied to Fig. 3 at the same location with different intensity levels as shown in Fig. 4, where Fig. 4 (a) has 50% intensity and (b) has 100% intensity.

Figure 4. (a) Spotlight with 50% intensity. (b) Spotlight with 100% intensity.

The intensity of the light is expected to vary from image to image, given that they are taken at different points in time. As expected, differences in intensity gray level occur under different lighting conditions for the same image as shown in Figure 5 (a) and (b).

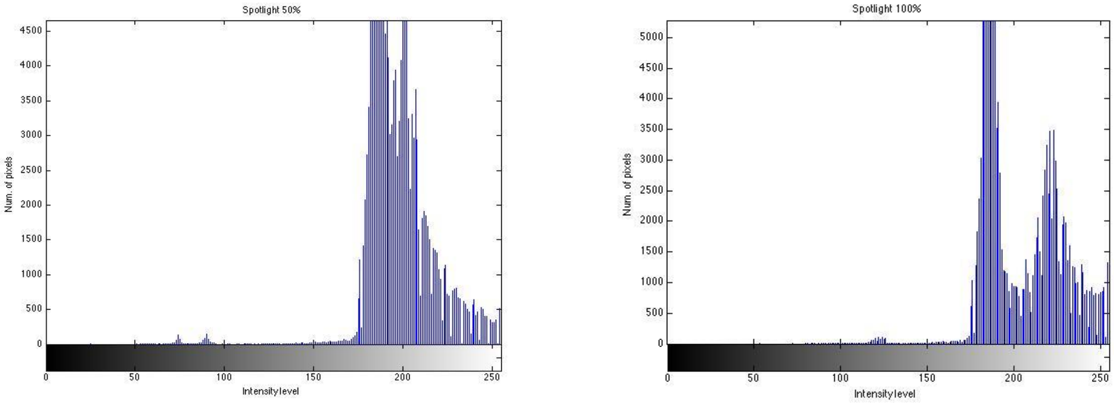

Figure 5. (a) Histogram of Figure 4 (a). (b) Histogram of Figure 4 (b).

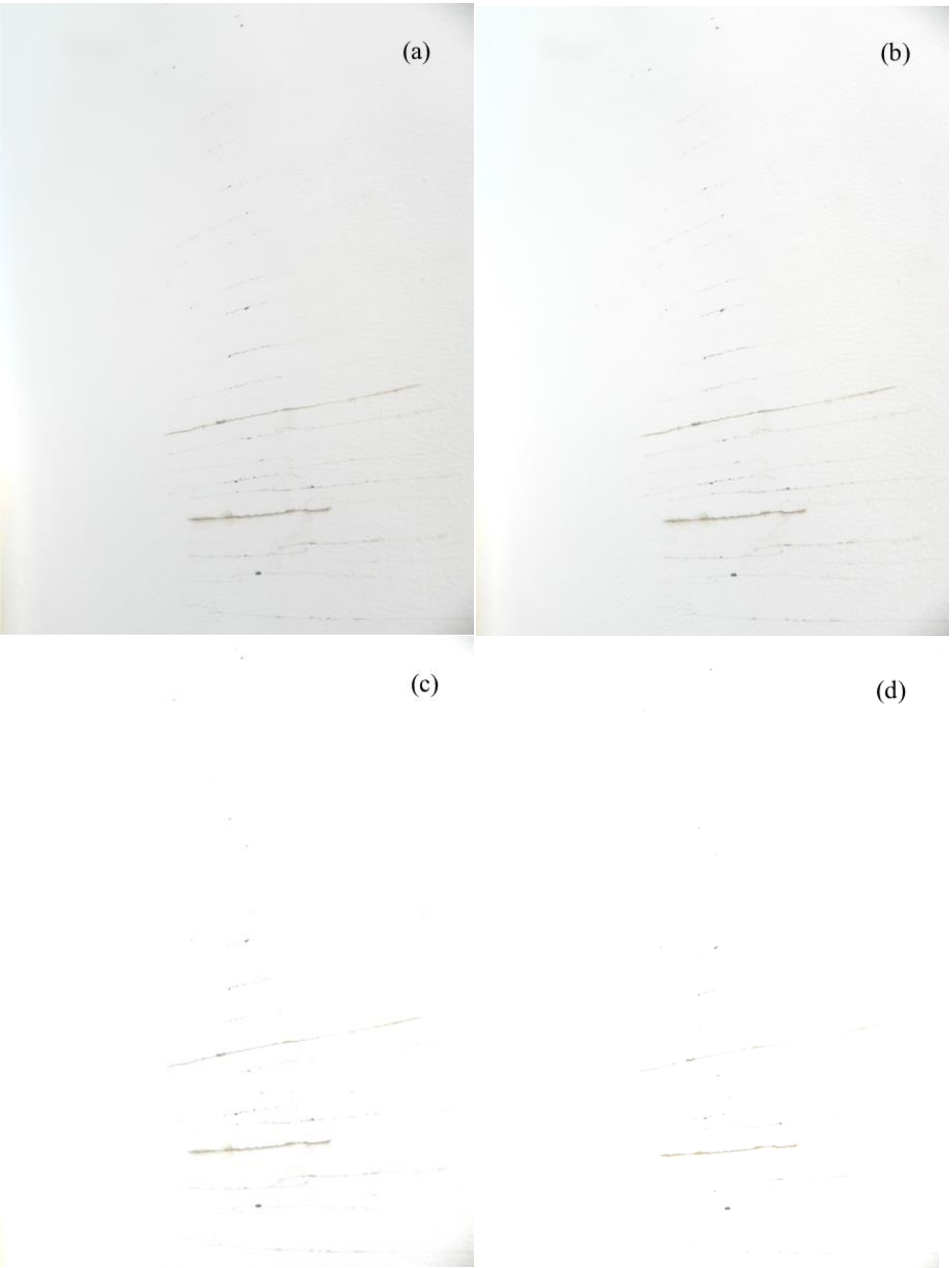

Figure 6. Infinite light vertically above the image (a)70% intensity, (b) 75% intensity, (c) 85% intensity, (d) 95% intensity

There were two ways to apply the infinite light, one of them is to keep the intensity level at a fixed number, say 90%, and rotate the light from east to west to simulate the position changes of the sun. The other way is to fix the position of the light resource vertically above the image and gradually increase its intensity from 50% to 100%. Our study showed that there was no significant impact when the intensity level is below 50% for infinite light. The first approach was tested and the infinite light did not generate any bright spots on the image when the light was moved away from being directly vertical above the image like direct sunlight during the middle of the day. Therefore, we focused on the second approach and the images with different intensity levels in Fig. 6. When the intensity level changed from 70% to 95%, the background become brighter and fewer cracks were visible to human eye.

All images were tested with the edge detection method and compared using the adaptive window size edge detection method. In addition, the crack classification method addressed in Chapter 5 was applied to the images to further validate the classification method in simulated field conditions as well as to confirm the lighting impact on crack recognition.

6.3 Results

6.3.1 Spotlight

The spotlight images in Fig. 4 were tested with the edge detection method (without the adaptive window) first and the results showed that the largest crack within the image was discontinuous due to voids/gaps generated by image segmentation as shown in Fig. 7 (a). The longest crack was formed by many small connected components with their centroid marked by a star. The adaptive window size method showed continuous and clear cracks. However, the spotlight also generated more noises with the adaptive window size methods as shown in Fig. 7 (b). It is because the adaptive window size method can capture more details within a small region, where the edges of the spotlight passed the image segmentation filters. Based on the major axis to minor axis length ratio method proposed in Chapter 5, the noise components generated by the spotlight were eliminated since the ratios were less than 5. The geometric properties of the top four largest connected components indicated that the image contains parallel hairline cracks. Since the orientation of the cracks was similar, the crack classification method defined it as parallel hairline cracks, which would be classified as stress cracks as defined in Chapter 4.3.1.

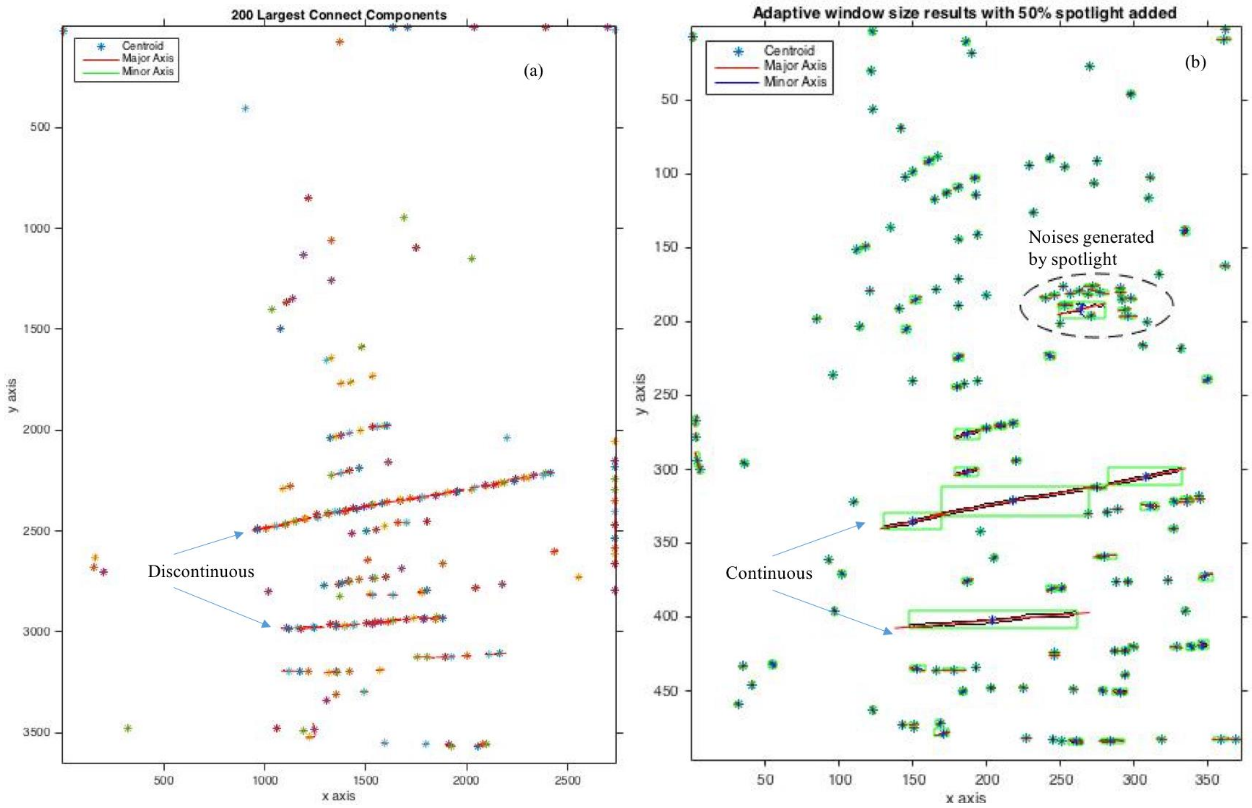

Figure 7. Results of 70% spotlight (a) edge detection method proposed in Chapter 3, (b) adaptive window size method

As the intensity level of the spotlight increased, the noise generated by the spotlight was more obvious and the continuity of the largest cracks was reduced as shown in Fig. 8. However, there was sufficient information to classify the crack. The noise generated by the spotlight was much easier to eliminate when the intensity level of the spotlight was stronger since the noise would be much closer to the contour of the spotlight as shown in Fig. 8. Besides the noise generated by spotlight, other connected components appeared as small discontinuous hairline cracks or background noise. However, there were still a large number of connected components with major axis to minor axis length ratio larger than 5 that were be able to determine the crack type as shown in Fig. 8. Although we could classify the crack type, the true full size of the parallel hairline cracks could not be easily determined. Therefore, extreme spotlight conditions should be avoided in field image acquisition.

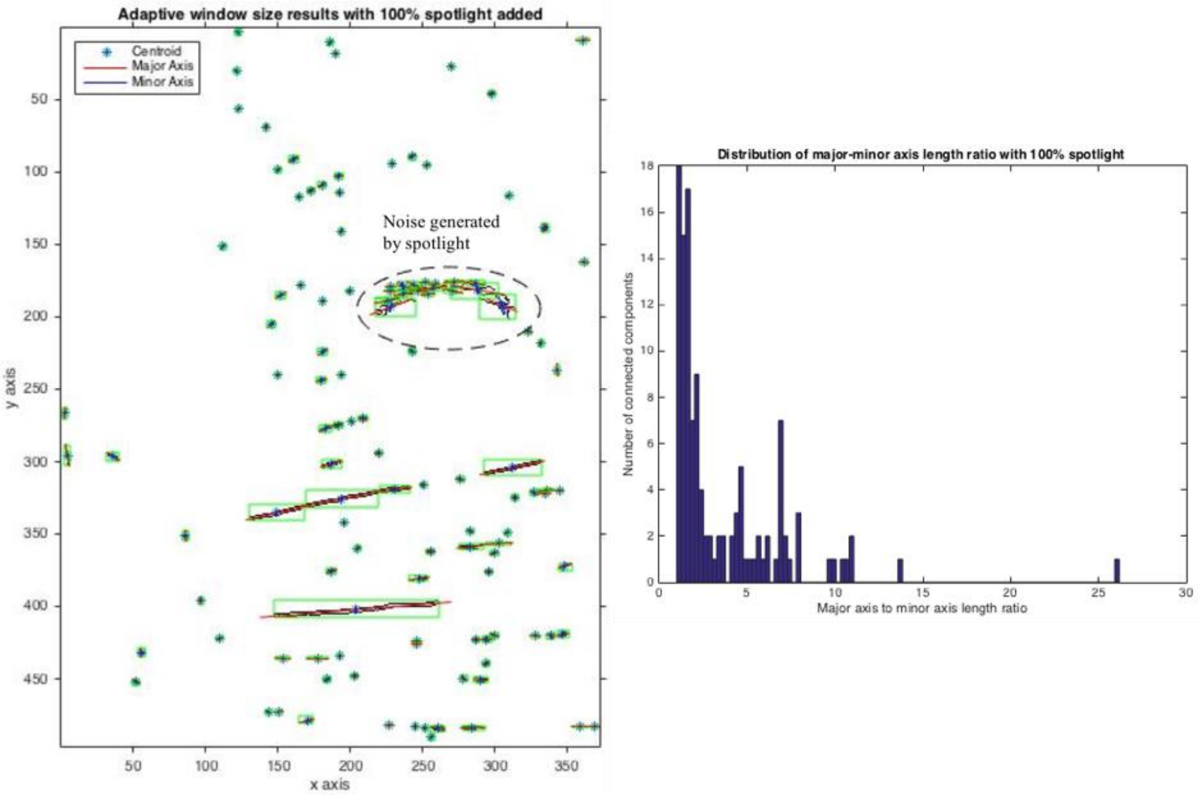

Figure 8. Results of 100% spotlight and histogram of major axis to minor axis length ratio

6.3.2 Infinite light

Unlike spotlights, infinite light was evenly distributed on the entire image and thus, the noise generated by the infinite light also affected the inspection results evenly. One type of noise that appeared in this condition was background noise with isolated small connected components (2-4 pixels). The other type of noise was discontinuous cracks since infinite light reduced the pixel intensity level along the cracks and more voids/gaps were created during image segmentation. Compared to the edge detection method, the adaptive window size method may have generated more small background noise (see Fig. 9) but it captured the large connected components, which is important in determining crack type and behavior (see Fig. 10).

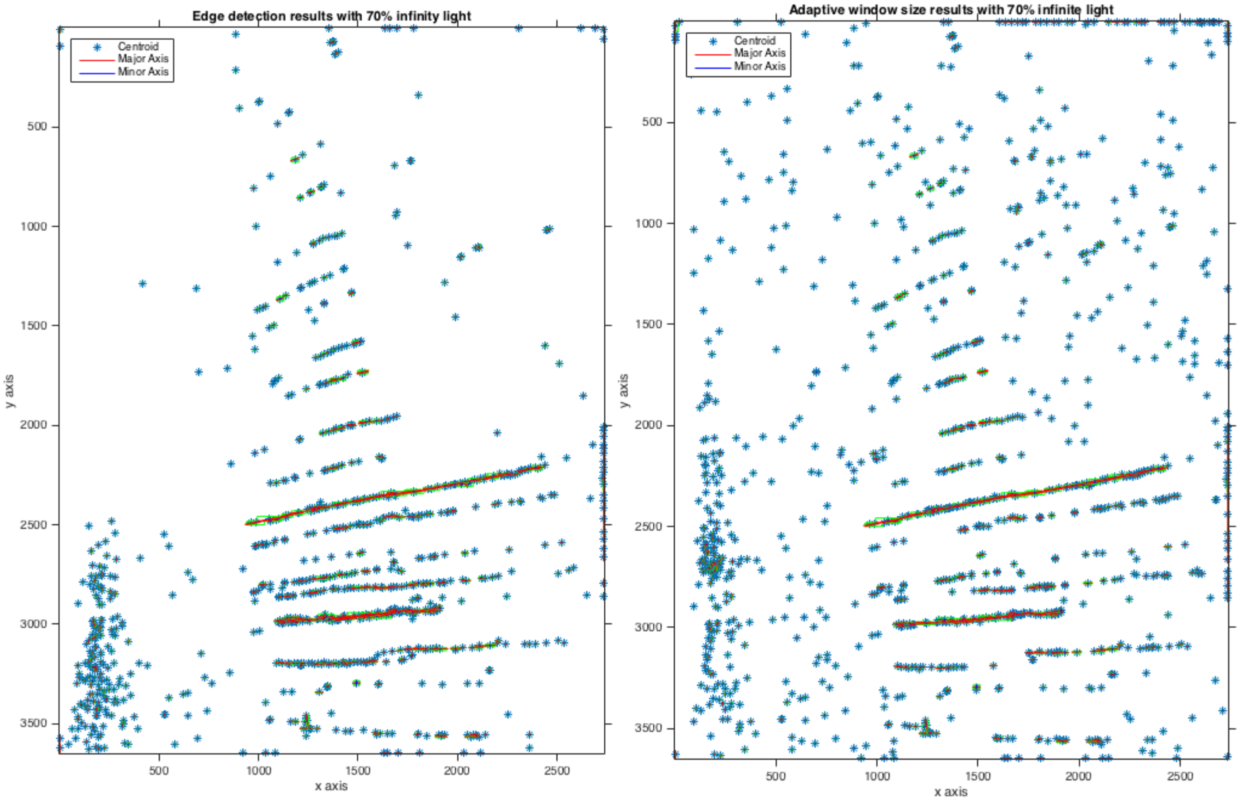

Figure 9. Results of 70% infinite light (a) edge detection, (b) adaptive window size

The largest crack captured by the adaptive window size method is nearly double the size of the largest crack captured by the edge detection method as shown in Fig. 10. In addition, the largest connected components captured by the adaptive window size method were longer hairline cracks since their major axis to minor axis length ratio was larger than those from the edge detection method (see Fig. 9). Also the adaptive window size method contained 10 more connected components with major axis to minor axis length ratio larger than 10. Thus, the adaptive window size method improved the accuracy of the inspection results and reduced the uncertainty of missing large connected components.

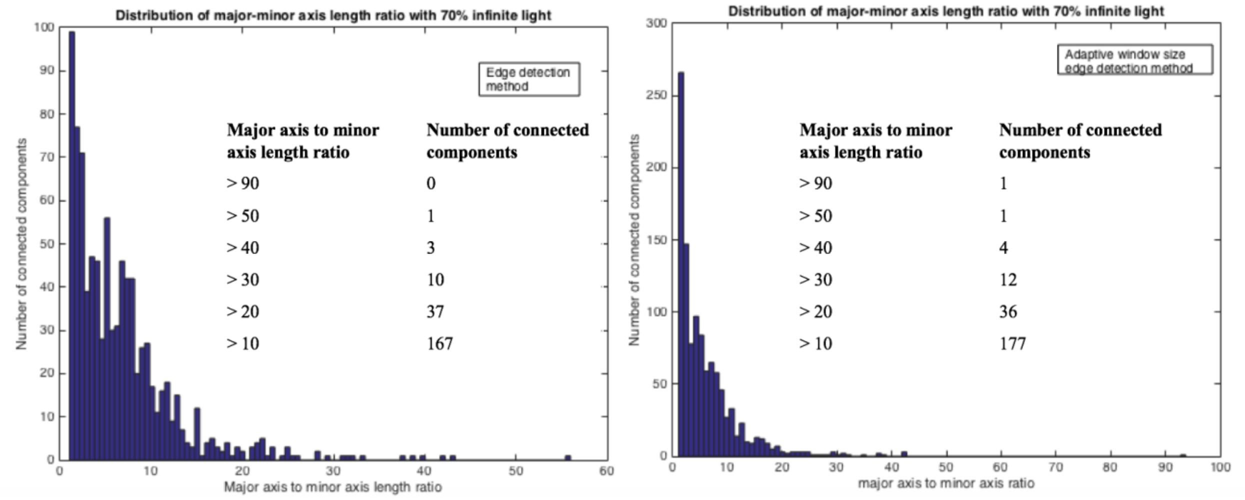

Major axis to minor axis length ratio	Number of connected components
> 90	0
> 50	1
> 40	3
> 30	10
> 20	37
> 10	167

Major axis to minor axis length ratio	Number of connected components
> 90	1
> 50	1
> 40	4
> 30	12
> 20	36
> 10	177

Figure 10. Results of 70% infinite light (a) edge detection, (b) adaptive window size

From these results, we can conclude that the infinite light added more noise that can be eliminated when the major axis to minor axis ratio is smaller than 5. The adaptive window size method resulted in more complete cracks with greater length. To address the impact of infinite light with different intensity levels, we compared the results based on the top 36 connected components, where their major axis to minor axis length ratio was greater than 20 as shown in Fig. 10 (b).

When the intensity level of the infinity light increased from 70% to 100%, the number of largest connected components detected decreased from 36 to 10 as shown in Fig. 11. The top 36 connected components were detected with infinity light at 85% intensity level. However, the major axis to minor axis length ratio was reduced for each connected component because of the strong infinity light. When the intensity level of the infinity light reached 90%, only 31 out of the

36 largest connected components could be detected. The number of components decreased to 17 at an intensity level of 95% and 10 at an intensity level of 100%. Similarly, the major axis to minor axis ratio also decreased as the intensity level of the infinity light increased. Even with the decrease in component detection, the crack was still detected and classified based on the geometric properties of its largest connected components. However, the true size of the parallel hairline crack could not be determined when the spotlight reached 100% intensity.

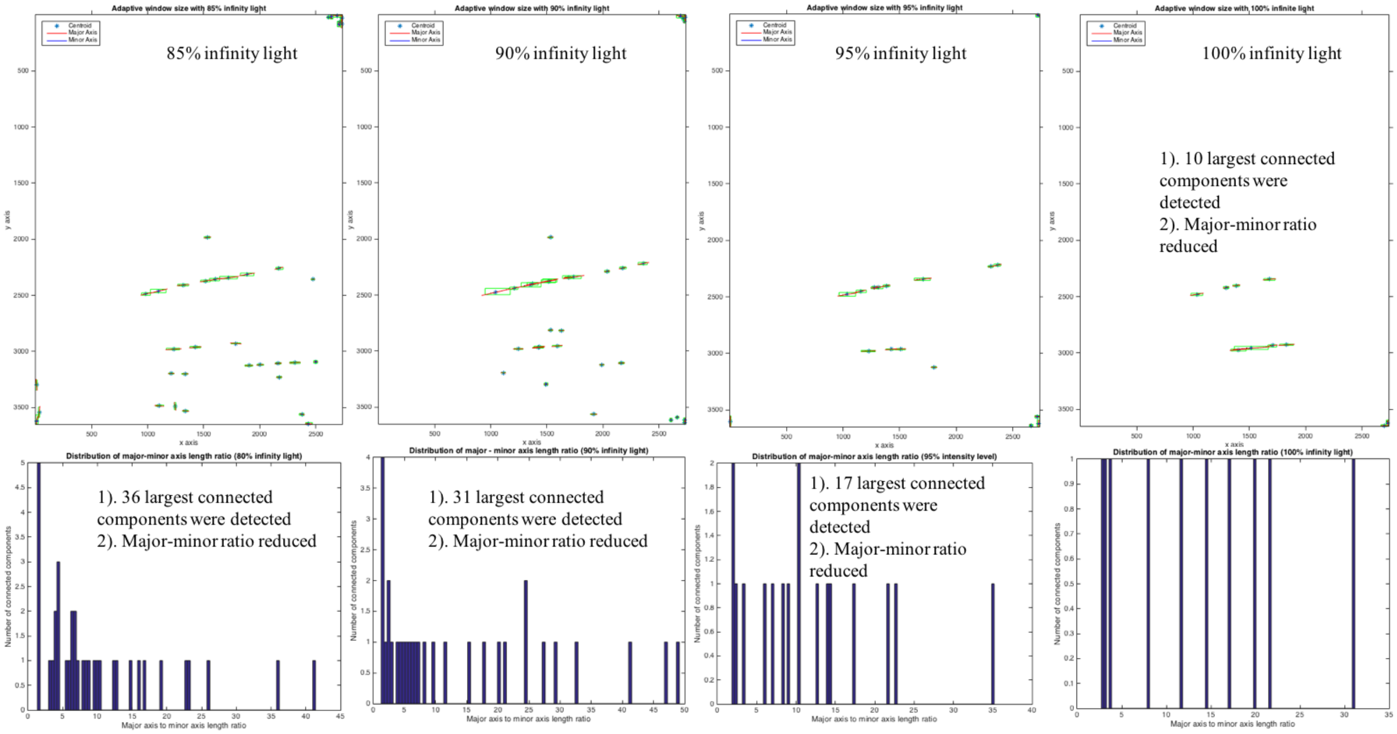

Figure 11. Results of infinity light at 85%, 90%, 95%, and 100% intensity.

6.3.3 Severe background noise

As described in section 6.3.1, a spotlight with an intensity level at 100% generated noise with the adaptive window size method since it captured more details from the image. The background noise had a major axis to minor axis length ratio smaller than 5 and its orientation was random as compared to the cracks. Thus, severe background noise was eliminated with the crack recognition and classification method proposed in Chapter 5.

When the intensity of infinity light increased, more background noise appeared since the infinity light reduced the intensity level of pixels evenly along the cracks. Gaps/voids may have also increased along the large cracks since the intensity level difference between the cracks and background noise may be reduced. The study in section 6.3.2 showed that the background noise was limited but intense and had a small major axis to minor axis length ratio. Therefore, background noise can be removed with the same method as the spotlight noise. Although we can still recognize the field cracks with extreme uneven lighting (100% intensity), the size of the true cracks could not be quantified as accurately as the field cracks without extreme uneven lighting. The study showed that a 75% intensity level of uneven lighting is the threshold of lighting at which the full cracks can be detected.

6.4 Conclusions

Uneven lighting and background noise were two major factors in the amount of uncertainty produced by image processing techniques. The uneven lighting was studied in section 6.2 with artificial spotlights and infinity light to represent field conditions. The results showed that the defects could be recognized and classified based on the method proposed in Chapter 5. The inspection results for the 100% intensity spotlight in Fig. 8 showed that the adaptive window size method could significantly reduce the uncertainty from the environment.

Severe background noise generated by the full intensity spotlight was eliminated based on its geometric properties. Thus, the method can also reduce the uncertainty generated by the adaptive window size edge detection method. The same method was applied to the background noise along the right bottom of the stress crack as shown in Fig. 4 in Chapter 5 and the severe background noise on the crazing crack in Fig. 5 in Chapter 5. Both results illustrated that the classification method can filter out severe background noise that significantly reduced the uncertainty associated with the inspection method.

Finally, the adaptive window size method offered more accurate detection results because the largest hairline cracks could be captured even with 100% intensity spotlight/infinity light. The adaptive window size method reduced the appearance of voids/gaps along the hairline cracks after edge detection. In addition, the background noise generated by the adaptive window size method was eliminated by the crack classification method proposed in Chapter 5. Thus, the uncertainties generated by image processing techniques were reduced with the combination of adaptive window size, edge detection, and shape-based crack classification.

6.5 References

[1] H. Zhang and J. Jackman, Feasibility of Automatic Detection of Surface Cracks in Wind Turbine Blades. *Wind Engineering*, vol. 38, no. 6, pp. 575-586, 2014.

[2] H. Zhang and J. Jackman, A feasibility study of wind turbine blade surface crack detection using an optical inspection method. *Renewable Energy Research and Applications (ICRERA), 2013 International Conference on*, DOI: 10.1109/ICRERA.2013.6749869. pp 847–852, 2013.

[3] R.C. *Gonzalez,* "Digital Image Processing Using MATLAB", *in Title of His Published Book,* 2nd ed., Upper Saddle River, N.J., Pearson Education, Inc. 2004

CHAPTER 7. GENERAL CONCLUSIONS

7.1 Contributions

Previous research in Chapter 3 has shown that the line detection method can be used for a quick-scan of WTBs and the edge detection method can detect cracks with uneven lighting and background noise. This research has shown that it is possible to use image processing techniques to automate routine inspections of WTBs. The proposed methods are a major advance in WTB inspection as compared to current O&M practices and can significantly improve the inspection results.

Another contribution is that we developed a second thresholding method for connected components that will significantly eliminate background noise. The threshold was computed by taking the top 10% of the component size distribution and then using the mean value of this subset as the threshold. We expect that this second thresholding method will be extensible to other inspection scenarios with significant environmental noise such as automated aircraft inspections and boat inspections.

The third contribution is that we developed a shape-based method that can recognize and classify cracks based on the geometric properties of (and between) large connected components. By doing so, the human error and variation between engineers can be reduced. In addition, the shape-based method can eliminate the background noise that remains after edge detection, further reducing the uncertainty.

The uncertainty was evaluated based on the number of largest connected components detected, the ability to eliminate high levels of background noise, and the accuracy of classifying the cracks.

Finally, the combination of adaptive window size, edge detection, and shape-based crack classification can be used to inspect images with complex field conditions that include severe uneven lighting and high levels of background noise. By doing so, the proposed method can be used in real-time field inspections. The proposed methods will help on-site technicians detect early defects like hairline cracks quickly so that O&M costs can be reduced and the available life of the wind turbine can be increased.

7.2 Future research and extensions

The analysis of more field images with the proposed methods would provide further validation of the robustness of the methods. The effectiveness of these methods should be studied in the context of real-time acquisition and analysis and in inspections while the blades rotate.

ACKNOWLEDGEMENT

The dissertation was completed with the support of my professors, family, and friends. I owe my gratitude to those who have made this dissertation possible and made my doctoral life at Iowa State University unforgettable.

First and foremost I would like to express my sincere gratitude to my advisor Dr. John Jackman for his expert guidance, tremendous mentorship, and insightful encouragement through my graduate school lifetime. I also thank him for bringing me to the Wind Energy Science, Engineering, and Policy program where I received a generous fellowship and inspirational international experiences.

In addition to my advisor, I would like to thank my committee: Dr. Meeker, Dr. Dayal, Dr. Matthew, and Dr. Peters, for not only their insightful comments, but also the hard questions, which enhanced my research from various perspectives.

The most special thanks belongs to my husband Nathan Jackson, for his understanding, endless love, and support through my graduate studies. His strong belief in women pursing higher education inspired me and I now extend the hard work to my professional life. In addition, I would like to thank our first baby who will be born three months after my graduation.

I will forever be thankful to my parents Qiping Zhang and Cheng’e Fan for teaching me to become a responsible, strong woman and to balance hard work with a rewarding family life. As the first generation in my family to go to college let alone obtain a doctoral degree, I could never have imagined these accomplishments without their support of my early education. I also thank my in-laws, Rob and Mary Jackson, for their patience and selfless support during the preparation of this dissertation.

The work was supported [in part] by the U.S. National Science Foundation through its Integrated Graduate Education and Research Traineeship (IGERT) Program, award 1069283.